学位論文（要約）

Electrical and Magnetic Properties of
Rare Earth Monoxide Epitaxial Thin Films

（希土類単酸化物エピタキシャル薄膜の電気・磁気特性）

平成 29 年 12 月博士（理学）申請

東京大学大学院理学系研究科

化学専攻

神永　健一

Electrical and Magnetic Properties of
Rare Earth Monoxide Epitaxial Thin Films

by

Kenichi KAMINAGA

Department of Chemistry

Graduate School of Science

The University of Tokyo

December 2017

Abstract

Rare earth elements form insulating sesquioxides (RE_2O_3, RE: Sc, Y, and lanthanides) with highly closed shell trivalent ions. Only a few elements such as Eu and Yb form thermodynamically stable rocksalt monoxides with divalent ions. Rare earth monoxides (REO) were obtained several decades ago by high pressure synthesis in the bulk polycrystalline form. Since then, almost no report has been made probably due to their poor chemical stability.

Recently, thin film growth technology has made significant progress. Especially, epitaxial growth technique using pulsed laser deposition (PLD) has enabled the synthesis of metastable materials in non-equilibrium conditions. Thus, it would be possible to stabilize unknown REOs in form of epitaxial thin film.

In this study, I have fabricated YO, LaO, and GdO epitaxial thin films by PLD method and investigated the electrical transport properties and magnetic properties of these REO thin films.

YO with divalent state (Y^{2+}: $[Kr]4d^1$) grew coherently on CaF_2 (001) substrate. The carrier density (n) and lattice constants of the YO thin film monotonically increased with decreasing oxygen partial pressure during deposition (P_{O2}). As a result, the resistivity (ρ) was tunable in a wide range of 10^{-3}-10^1 Ω.cm. The films with $n \geq 10^{20}$ cm^{-3} showed metallic conduction with positive dρ/dT slopes, whereas those with $n \leq 10^{20}$ cm^{-3} were found to be semiconducting with negative dρ/dT. The semiconducting YO films exhibited a kink in absorption spectra, which is characteristic of Mott insulators. These results suggest that the stoichiometric YO film is a Mott insulator and

undergoes an insulator-metal transition by doping carrier electrons. The metallic YO film showed positive magnetoresistance with a sharp dip around 0 T originating from the weak antilocalization effect, suggesting significant spin-orbit interaction.

Compressively strained LaO thin films grew coherently on YAlO$_3$ substrates regardless of P_{O2}. The delocalized $5d^1$ electrons from La^{2+}: [Xe]$5d^1$ lead to high carrier density of ~10^{22} cm^{-3}. The resistivity *vs.* temperature curve of the LaO (001) epitaxial thin film showed not only metallic conduction but also superconductivity with onset T_c^{onset} of 4.56 K and zero resistance T_c^{zero} of 3.70 K. Magnetization measurements proved almost full volume fraction, implying bulk superconductivity. Considering from the chemical trend of LaX, the transition temperature of LaO should be below 1 K. The density of state at the Fermi level $N(E_F)$ was evaluated to be four times as large as the theoretical values of LaX series. According to the BCS theory, the relatively high T_c of LaO can be rationalized by high $N(E_F)$. The tensilely strained LaO thin film on LaAlO$_3$ substrate showed higher T_c (T_c^{onset} = 5.24 K and T_c^{zero} = 4.59 K) than that of compressively strained films on YAlO$_3$ substrate. Although $N(E_F)$ and Debye temperature θ_D of the tensilely strained film were almost comparable to those of compressively strained film, the electron-phonon coupling parameter λ_{e-p} was the largest for the tensilely strained film, suggesting an influence of lattice strain on T_c through electron-phonon interaction.

GdO grew coherently on CaF$_2$ (001) substrate. GdO possesses Gd^{2+} with half-filled $4f$ orbital([Xe]$4f^75d^1$) like ferromagnetic semiconductor EuO. The electrical transport properties of the GdO film can be controlled from semi-insulating to metallic state with P_{O2}. Both semi-insulating and metallic GdO films showed ferromagnetism with Curie temperature (T_C) of around 320 K, which is the highest value among Gd binary compounds reported so far. The electron carrier doping through incorporation of oxygen

vacancies was ineffective to increase T_C. The electron configuration of GdO possibly contributes to such high T_c through e.g. RKKY interaction. The shape of M-H curve corresponds well to that of anomalous Hall effect (AHE) as a function of H. Both loops showed clear hysteresis even at 300 K.

In conclusion, I have synthesized REO epitaxial thin films (RE = Y, La and Gd) with unusual valence states of RE^{2+} by PLD and investigated their electrical and magnetic properties. YO was suggested to be a Mott insulator with $4d^1$ configuration and the electrical transport properties could be tuned from semi-insulating to metallic states by electron doping. The compressively strained LaO thin film on $YAlO_3$ substrate exhibited superconductivity with onset T_c of 4.56 K, which is highest among rocksalt LaX due to the large density of state at the Fermi level. Higher onset T_c of 5.24 K was observed in the tensilely strained LaO thin film on LAO substrate, probably reflecting the effect of lattice strain on T_c through electron-phonon interaction. GdO was proved to be a room temperature ferromagnetic semiconductor from the hysteretic M-H, AHE-H loops observed at 300 K. In the present study, I established the method to synthesize REO thin films with unusual valence states of RE^{2+} and demonstrated their unique electronic properties, paving the way for electronics utilizing REO.

Contents

Chapter 3:   Epitaxial thin film growth of YO, LaO, and GdO 46

Chapter 4:   Semiconducting properties of YO 57

Chapter 1:
General introduction

1.1 Introduction of Rare Earth oxides

1.1.1 Chemical similarities of Rare Earth elements

Rare Earth (RE) elements are a group of 17 found in Group 3 of the periodic table, including scandium ($_{21}$Sc), yttrium ($_{39}$Y), and 15 elements, called as "lanthanides", from lanthanum ($_{57}$La) through lutetium ($_{71}$Lu). These 17 Rare Elements have chemical similarities arising from similar electron configuration and ionic radii.

Table 1.1 shows the electron configuration of RE atoms and ions [1,2]. Here, [Ar], [Kr], and [Xe] indicate the electron configuration of noble gases, are shown below. Each RE atom or ion possess electron configuration in which the orbital electrons in the higher order are added to the orbitals of these noble gases.
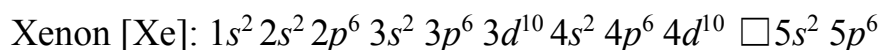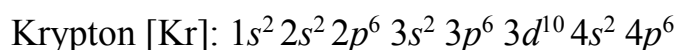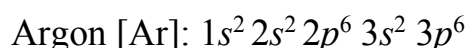
Argon [Ar]: $1s^2\,2s^2\,2p^6\,3s^2\,3p^6$

Krypton [Kr]: $1s^2\,2s^2\,2p^6\,3s^2\,3p^6\,3d^{10}\,4s^2\,4p^6$

Xenon [Xe]: $1s^2\,2s^2\,2p^6\,3s^2\,3p^6\,3d^{10}\,4s^2\,4p^6\,4d^{10}\,\square\,5s^2\,5p^6$

Table 1.1 Electron configurations of *RE* elements and ions [1,2].

RE elements	Atom	RE^{3+}	RE^{2+}	RE^{4+}
Sc	$[Ar]3d^14s^2$	$[Ar]$	$[Ar]3d^1$	
Y	$[Kr]4d^15s^2$	$[Kr]$	$[Kr]4d^1$	
La	$[Xe]5d^16s^2$	$[Xe]$	$[Xe]5d^1$	
Ce	$[Xe]4f^15d^16s^2$	$[Xe]4f^1$	$[Xe]4f^15d^1$	$[Xe]$
Pr	$[Xe]4f^36s^2$	$[Xe]4f^2$	$[Xe]4f^3$	$[Xe]4f^1$
Nd	$[Xe]4f^46s^2$	$[Xe]4f^3$	$[Xe]4f^4$	$[Xe]4f^2$
Pm	$[Xe]4f^56s^2$	$[Xe]4f^4$	$[Xe]4f^5$	
Sm	$[Xe]4f^66s^2$	$[Xe]4f^5$	$[Xe]4f^6$	
Eu	$[Xe]4f^76s^2$	$[Xe]4f^6$	$[Xe]4f^7$	
Gd	$[Xe]4f^75d^16s^2$	$[Xe]4f^7$	$[Xe]4f^75d^1$	
Tb	$[Xe]4f^96s^2$	$[Xe]4f^8$	$[Xe]4f^9$	$[Xe]4f^7$
Dy	$[Xe]4f^{10}6s^2$	$[Xe]4f^9$	$[Xe]4f^{10}$	$[Xe]4f^8$
Ho	$[Xe]4f^{11}6s^2$	$[Xe]4f^{10}$	$[Xe]4f^{11}$	
Er	$[Xe]4f^{12}6s^2$	$[Xe]4f^{11}$	$[Xe]4f^{12}$	
Tm	$[Xe]4f^{13}6s^2$	$[Xe]4f^{12}$	$[Xe]4f^{13}$	
Yb	$[Xe]4f^{14}6s^2$	$[Xe]4f^{13}$	$[Xe]4f^{14}$	
Lu	$[Xe]4f^{14}5d^16s^2$	$[Xe]4f^{14}$	$[Xe]4f^{14}5d^1$	

In the lanthanide atom, the $4f$ orbital enters the ☐ position of [Xe] and $6s^2$ is added to the outermost shell. In addition, in La, Ce, Gd, and Lu atoms, $5d^1$ electron enters between $5p^6$ and $6s^2$. All *RE* atoms possess two *s* electrons in the outermost shell, similar to alkaline earth atoms.

Figure 1.1 shows the relationship between the 6-coordinated ionic radius and the atomic number including *RE* elements [3,4]. Contradict to general trend, ionic radii of lanthanide trivalent ions become smaller as the atomic number increases; this phenomenon is called as "lanthanide contraction".
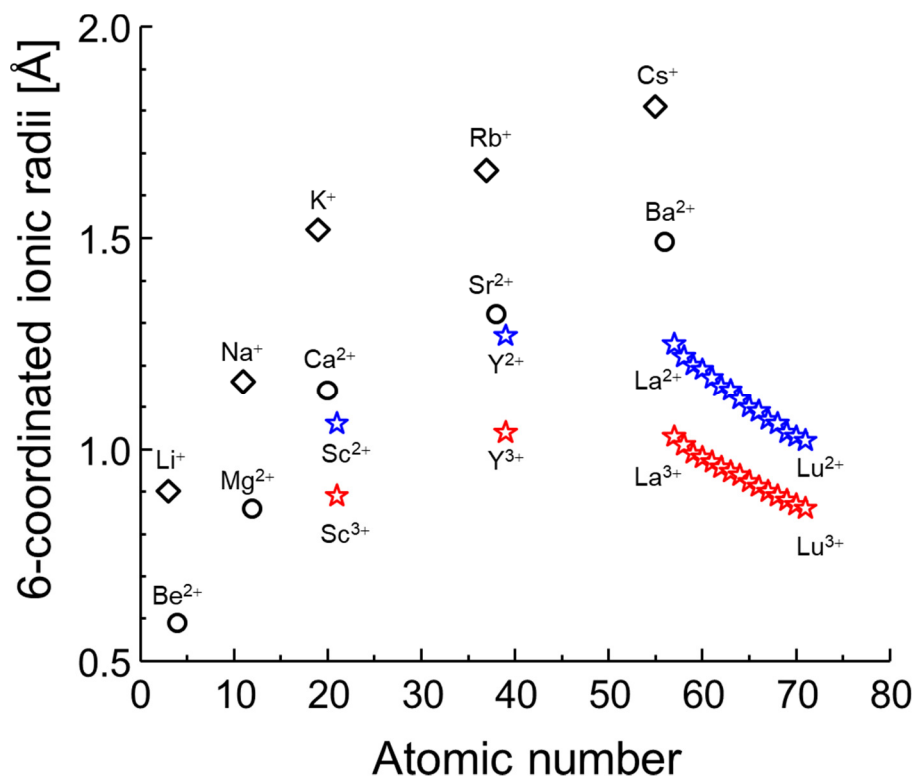
Figure 1.1   6-coordinated ionic radii of RE^{2+}(blue star), RE^{3+}(red star),   alkali metal (diamond), and alkali earth metal (circle) [3,4].
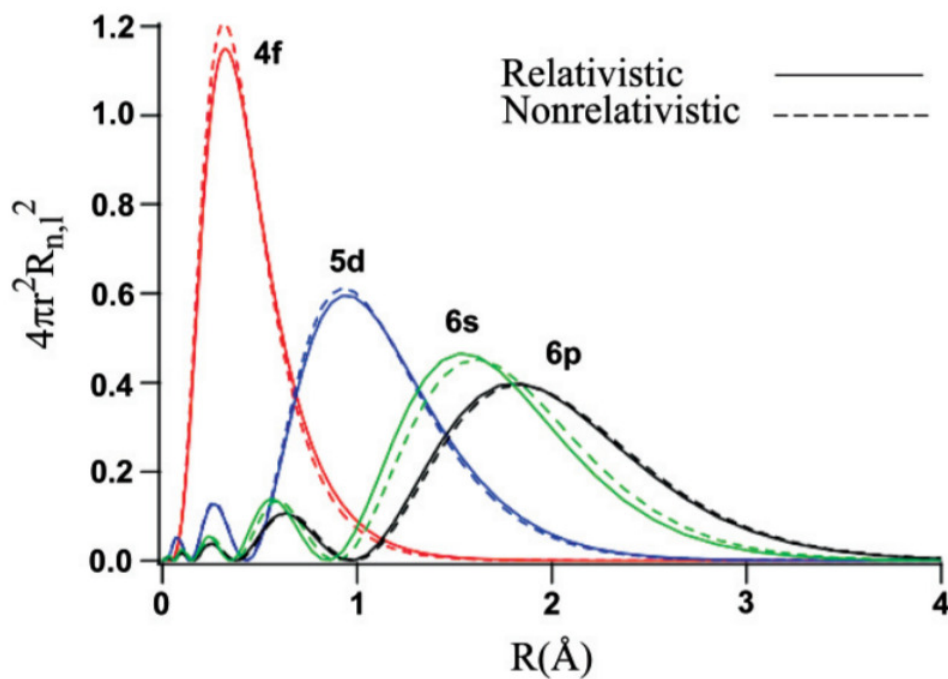

Figure 1.2   Calculated radial distribution functions for Sm^{3+}.   Reprinted with permission from [5]. Copyright 2004 by Royal Society of Chemistry.

Figure 1.2 plots the radial wavefunctions of 4f, 5s, 5p, 6s orbitals for Sm^{3+} as a function of the distance from the nucleus [5]. The 4f orbital is located closer to the nucleus, but shielding of nuclear charge by 4f orbital is insufficient due to the characteristic shapes of 4f orbital. Therefore, in lanthanide ions, the outer $5s^2 5p^6$ electron cloud penetrates the internal 4f orbital and feels strong attractive Coulomb force from the nuclear positive charges. The ionic radii of 15 lanthanide elements ranging from La^{3+} (1.03 Å) to Lu^{3+} (0.861 Å), Sc^{3+} (0.745 Å), and Y^{3+} (0.900 Å) are close to each other in the difference range of only 0.3 Å. According to the following empirical formula reported by Y.Q. Jia [4], the unknown 6-coordinated ionic radii of RE^{2+} can be calculated from those of RE^{3+}, as shown in Fig. 1.1

$$RE^{3+}/RE^{2+} = 0.842 + 0.0016\, N_f \quad (1.1)$$

where N_f is the number of the 4f electrons in RE^{3+}.

One remarkable chemical similarity between RE elements is that the trivalent state (RE^{3+}) is generally the most stable in aqueous solution and solid state. Table 1.2 shows the redox potential E^0 of RE ions [6]. RE metals are more reductive than alkali metals ($-E^0$ = 2.7 - 3.0 V) and alkali earth metals ($-E^0$ = 2.7 - 2.9 V), and they are much less reductive than aluminum ($-E^0$ = 1.66 V). Eu and Yb have smaller $-E^0$ values than other RE ions, and thus they are more reductive. These two small $-E^0$ values for $RE^{3+} + e^- \rightarrow$ RE^{2+} indicate that the divalent state is relatively stable. Similarly, the relatively small $-E^0$ value of $RE^{4+} - e^- \rightarrow RE^{3+}$ in Ce indicates that Ce^{4+} is the only RE ion that can exist stably in aqueous solution as tetravalent state.

Table 1.2 Redox potential E^0 of *RE* ions [6]. Parentheses and * indicate the estimated values and the values in tetrahydrofuran, respectively.

	Sc	Y	La	Ce	Pr	Nd	Pm	Sm	Eu
$RE^{3+}+ 3e^- \rightarrow RE$	− 2.03	− 2.37	− 2.37	− 2.34	− 2.35	− 2.32	− 2.29	− 2.30	− 1.99
$RE^{3+}+ e^- \rightarrow RE^{2+}$			(− 3.1)	(− 3.2)	(− 2.7)	− 2.6*	(− 2.6)	− 1.55	− 0.34
$RE^{4+}+ e^- \rightarrow RE^{3+}$				1.70	(3.4)	(4.6)	(4.9)	(5.2)	(6.4)
	Gd	Tb	Dy	Ho	Er	Tm	Yb	Lu	
$RE^{3+}+ 3e^- \rightarrow RE$	− 2.29	− 2.30	− 2.29	− 2.33	− 2.31	− 2.31	− 2.22	− 2.30	
$RE^{3+}+ e^- \rightarrow RE^{2+}$	(− 3.9)	(− 3.7)	− 2.5*	(− 2.9)	(− 3.1)	− 2.3*	− 1.05		
$RE^{4+}+ e^- \rightarrow RE^{3+}$	(7.9)	(3.3)	(5.0)	(6.2)	(6.1)	(6.1)	(7.1)	(8.5)	

Figure 1.3 shows the values of the *n*-th ionization energy I_n for *RE* elements [6]. The much larger $I_1+I_2+I_3+I_4$ values than $I_1+I_2+I_3$ values in *RE* elements indicates that the trivalent states are generally most stable. The relatively high stability of divalent Sm, Eu, and Yb states can be attribute to the larger I_3 values of these ions. The divalent states of Eu and Yb have the half-filled and the completely filled 4*f* orbital, respectively, which also contribute to their stability.
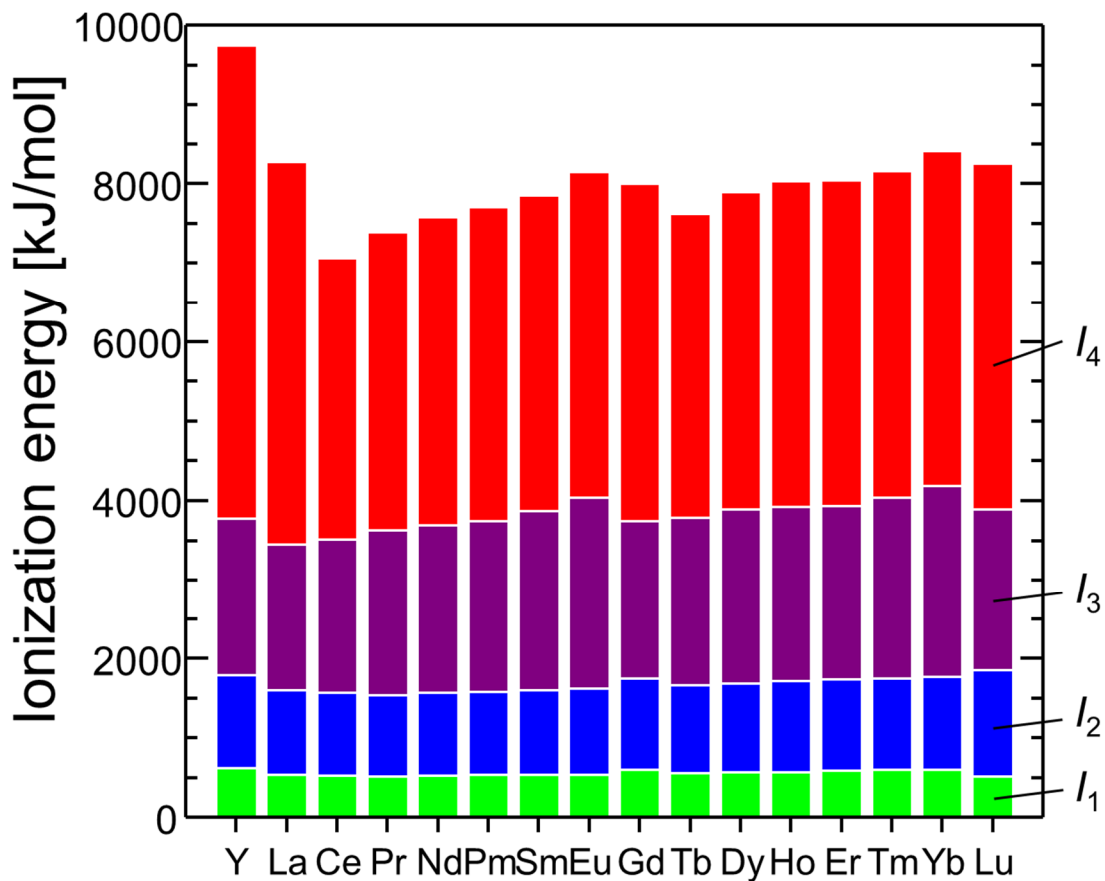
Figure 1.3 n th (n = 1-4) ionization energy of *RE* elements [6].

1.1.2 Characteristics of Rare Earth oxides

1.1.2.1 Crystal structure of Rare Earth oxides

In ambient atmosphere, *RE* metals vigorously react with oxygen and form oxides [1,7]. These oxides are thermally stable, and the final stoichiometry depends on the reaction temperature and the oxygen pressure. *RE* oxides are composed of ionic bonds between *RE* and oxide ions. Due to the stability of trivalent ions with closed shell, *RE* metals generally form sesquioxide (RE_2O_3) phases.

RE_2O_3 phase takes three crystal structures up to around 2000 °C [8], A-type, B-type, and C-type, and two crystal structures over 2000 °C, H-type, X-type, as shown in Fig.

1.4. A-type belongs to hexagonal system ($P32/m$), in which each RE ion is surrounded by seven oxide ions (7-coordinated) [Fig.1.4 (a)]. B-type belongs to monoclinic system ($C2/m$) like distorted A-type structure, and the RE ion is 6 or 7-coordinated [Fig.1.4 (b)]. C-type belongs to cubic system ($Ia3$), and the RE ion is 6-coordinated [Fig.1.4 (c)]. H-type and X-type belong to hexagonal system ($P6_3/mmc$) [Fig.1.4 (d)] and cubic system ($Im3m$) [Fig.1.4 (e)], respectively. C-type structure also is called as bixbyite structure, and RE_2O_3 forms C-type structure except for light elements (RE = La, Ce, Pr, Nd), as shown in Fig. 1.5.
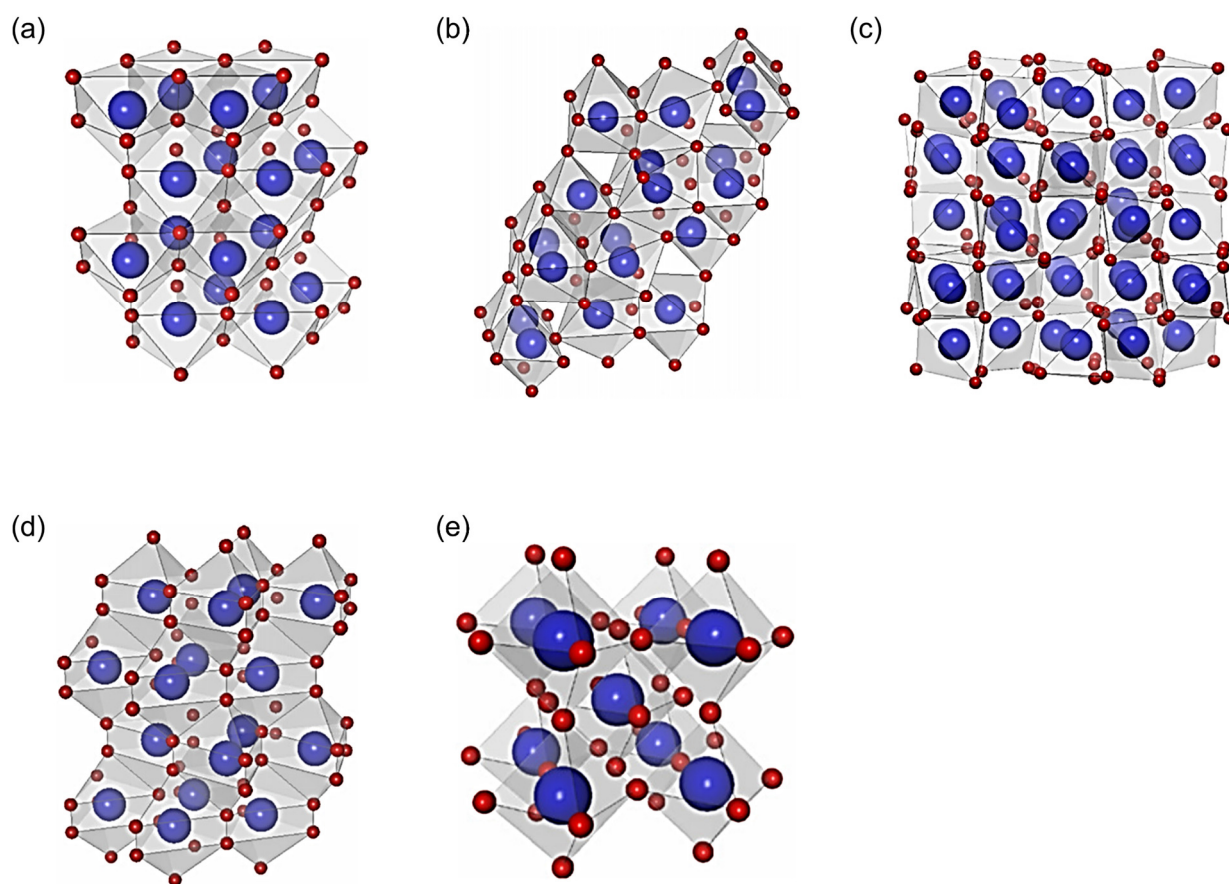

Figure 1.4 Crystal structure of RE_2O_3 (a) A-type, (b) B-type, (c) C-type, (d) H-type, (e) X-type. Reprinted with permission from [8]. Copyright 2007 by Elsevier.
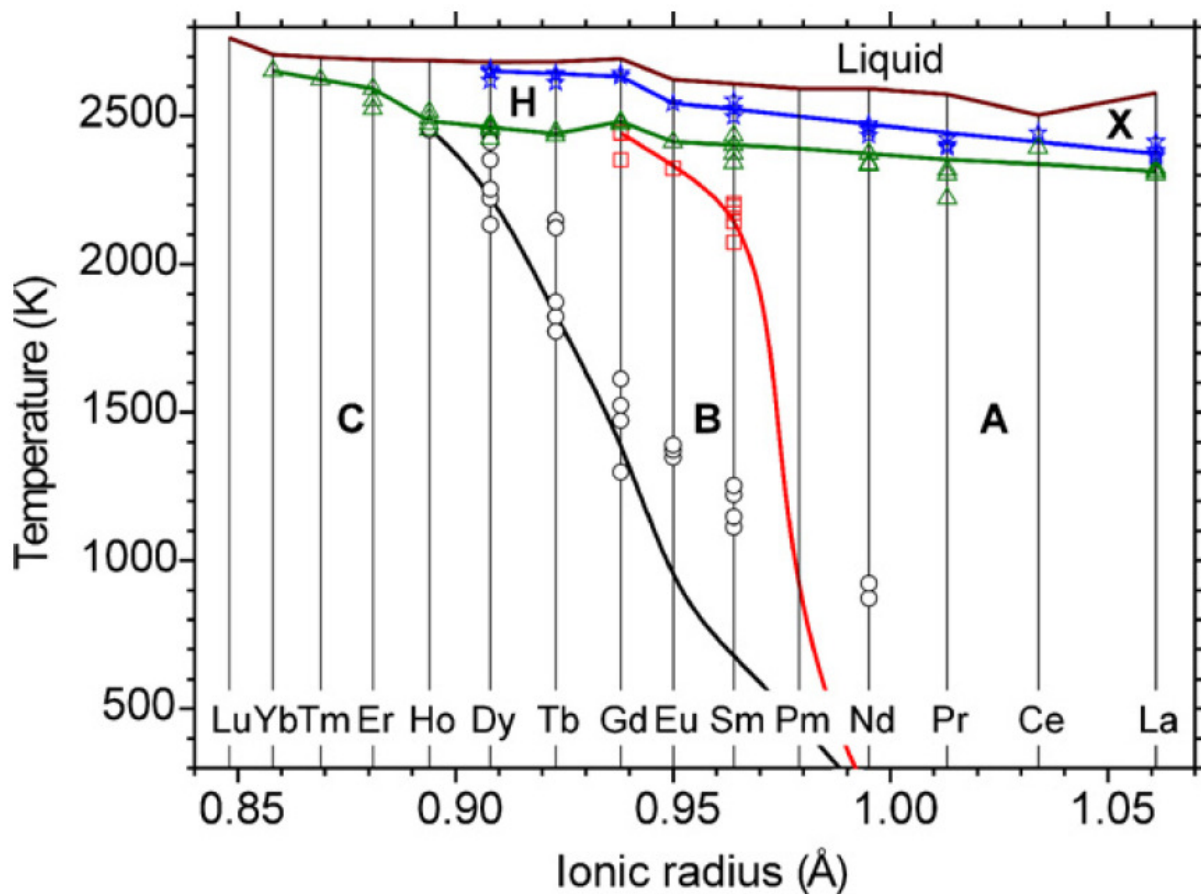
Figure 1.5 The scheme of polymorphic transformations in RE_2O_3. Reprinted with permission from [8]. Copyright 2007 by Elsevier.

Dioxide (REO_2) phase is observed among oxides of Ce, Pr, and Tb [1,7]. They have fluorite structure ($Fm3m$), and the removal of oxygen ions in each unit cell results in the crystal lattice of C-type RE_2O_3.

Among monoxide (REO) phases, EuO with rocksalt structure ($Fm3m$) is the only compound whose physical properties are widely researched [1,7]. Figure 1.6 shows the phase diagram of Eu-O system [7,9]. As seen from the figure, Eu_3O_4 phase with Eu^{2+}/Eu^{3+} mixed valence also exists, whose structure belongs to orthorhombic system ($Pnam$).
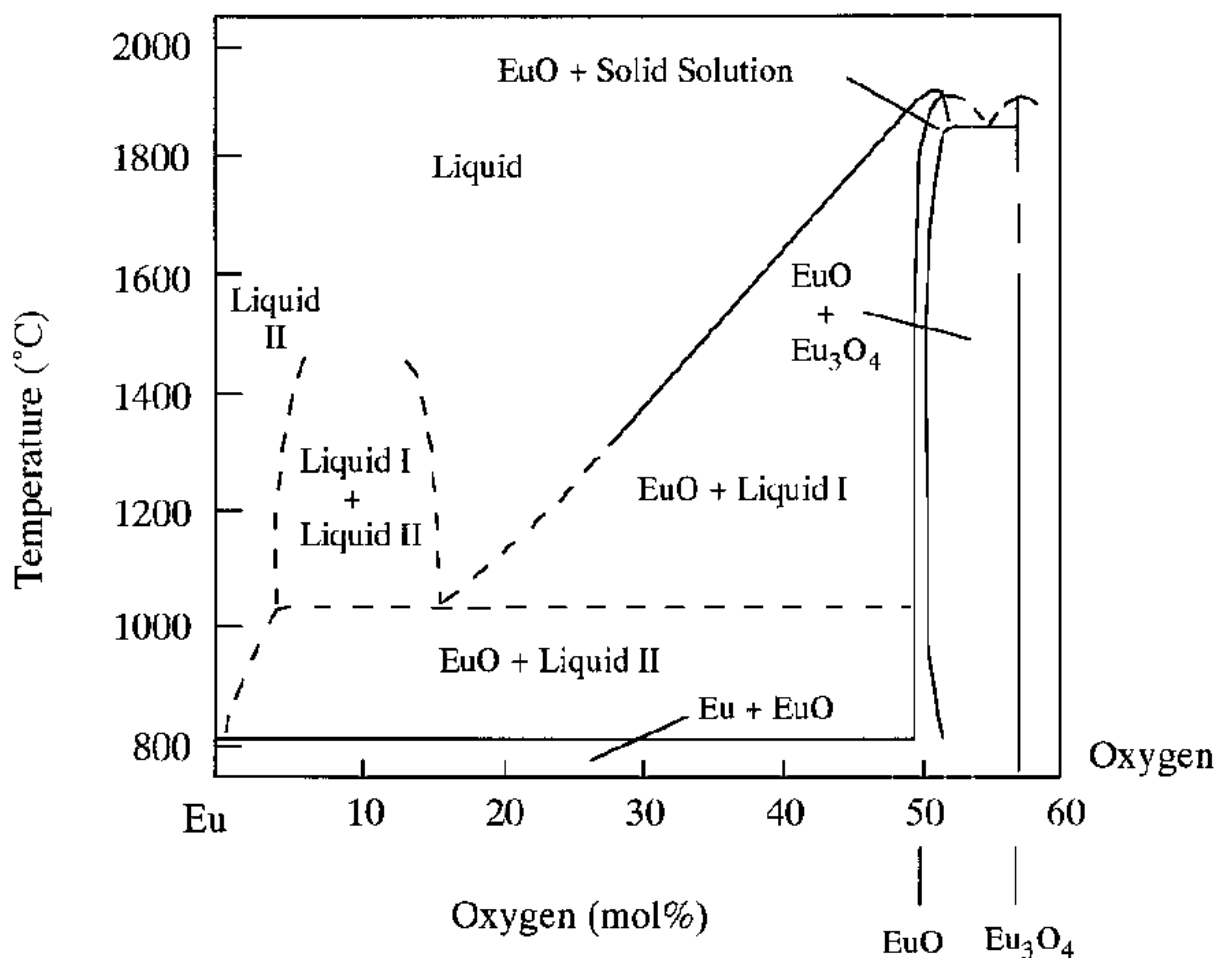
Figure 1.6 A phase diagram in the Eu-Eu$_3$O$_4$ region. Reprinted with permission from [7]. Copyright 1998 by American Chemical Society.

1.1.2.2 Chemical properties of Rare Earth oxides

RE$_2$O$_3$ phases are easily available and widely used as starting materials for synthesis of various compounds containing *RE*. *RE*$_2$O$_3$ takes crystal structures with relatively small atomic packing factor, which lead to the high reactivity.

RE ions have chemical properties similar to alkaline earth ions, and *RE* oxides are basic oxides. Therefore, *RE*$_2$O$_3$ easily dissolves into most of acidic aqueous solutions including organic acids and then forms salts [1]. CeO$_2$ is stable to these acids but dissolves in reducing agents, such as H$_2$O$_2$, when heated under the coexistence of acid.

9

Figure 1.8 shows standard Gibbs energy of formation (ΔG^o) of sesquioxides [7, 10]. RE_2O_3 has close values, but they are divided into two groups from La to Gd and from Dy to Lu. Sc and Y belong to the latter group. Contradict to these trends, Yb_2O_3 belongs to the former group. The ΔG^o value of Eu_2O_3 is close to that of Al_2O_3, which deviates from the chemical trend.

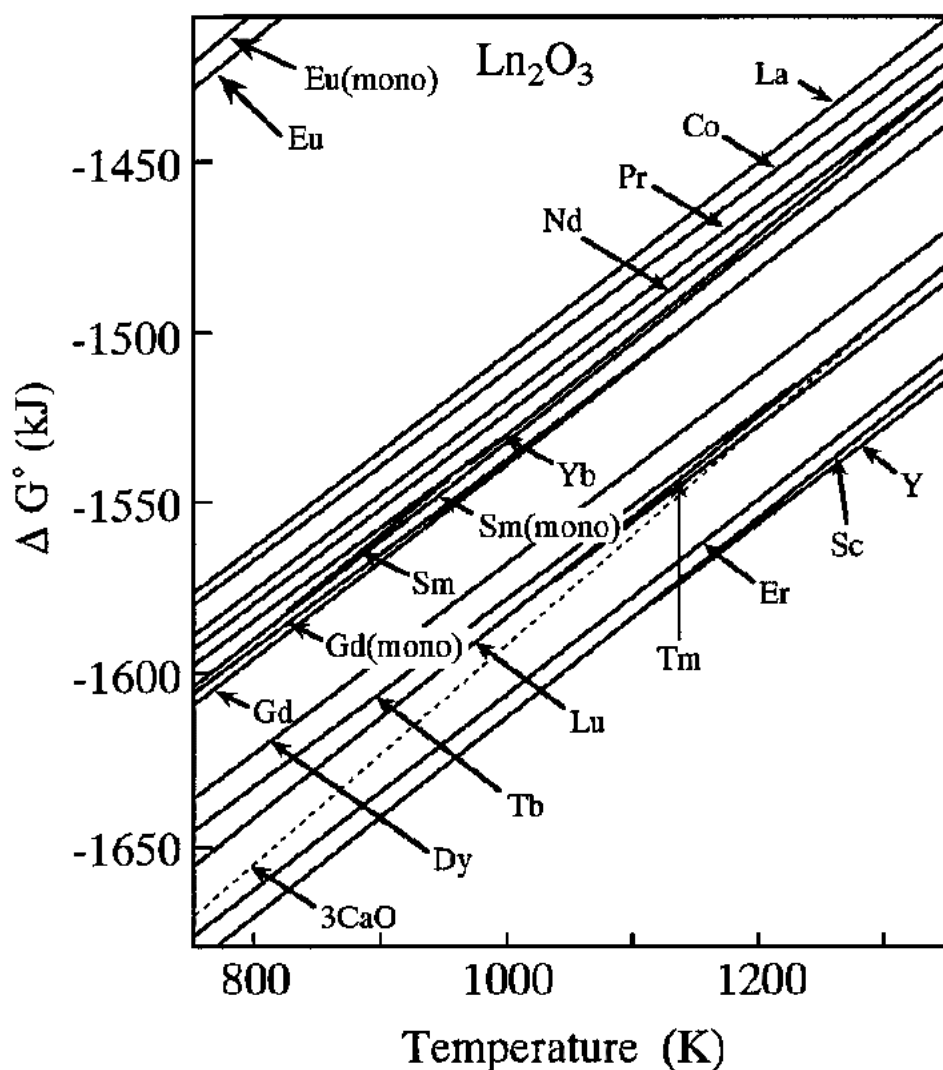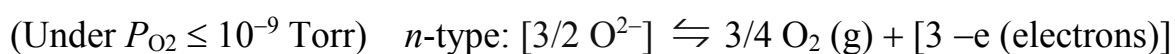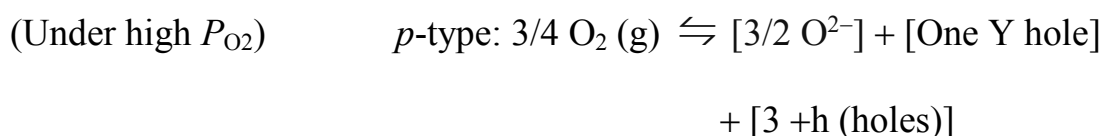Figure 1.6 Standard Gibbs energy of formation of RE_2O_3. Reprinted with permission from [7]. Copyright 1998 by American Chemical Society.

The crystal lattice energy of C-type RE_2O_3 tends to become smaller as the ionic radius becomes larger due to Coulomb attraction between RE^{3+} and O^{2-}. Indeed, La_2O_3 has the smallest crystal lattice energy of 1.25×10^4 kJ/mol and Lu_2O_3 has the highest value of 1.37×10^4 kJ/mol [6]. These values are smaller than that of Mn_2O_3 with the same C-type structure, 1.51×10^4 kJ/mol. As for the melting point, which is related to crystal lattice energy, La_2O_3 shows the smallest value of 2305 K and Lu_2O_3 shows the highest value of 2490 K [1].

1.1.2.3 Physical properties of Rare Earth oxides

The bandgap of RE_2O_3 is as large as 4.4 - 5.5 eV [11], and thus RE_2O_3 is highly insulating similar to diamond (resistivity $> 10^{13}$ Ω.cm [12]) at room temperature. However, above 1000 °C, RE_2O_3 shows semiconducting properties depending on oxygen partial pressure (P_{O2}). For example, Y_2O_3 becomes p-type semiconductor under high P_{O2} and n-type semiconductor under $P_{O2} \leq 10^{-9}$ Torr, as follows [1].

(Under high P_{O2}) p-type: 3/4 O_2 (g) $\leftrightarrows$ [3/2 O^{2-}] + [One Y hole]

+ [3 +h (holes)]

(Under $P_{O2} \leq 10^{-9}$ Torr) n-type: [3/2 O^{2-}] $\leftrightarrows$ 3/4 O_2 (g) + [3 −e (electrons)]

Ferromagnetism has not been reported for RE oxides except for EuO and Eu_3O_4 [7]. As described in detail later, EuO shows ferromagnetic properties with a Curie temperature of 69 K. Eu_3O_4, possessing one Eu^{2+} ion and two Eu^{3+} ions in the chemical formula, shows ferrimagnetic properties with a Néel temperature of 77 K.

Some RE oxides are reported to show antiferromagnetism [7,13]. $PrO_{2.0}$ exhibits antiferromagnetic ordering with a Néel temperature of 14 K. Single crystalline Gd_2O_3, Dy_2O_3, Er_2O_3, and Yb_2O_3 are antiferromagnetic with Néel temperatures of 3.9, 1.2, 3.4,

and 2.3 K, respectively. Terbium oxides with compositions of Tb_2O_3 (B-type and C-type), $TbO_{1.715}$, $TbO_{1.823}$ and $TbO_{2.0}$ shows antiferromagnetism with Néel temperatures of 2 K, 7 K, 7K , 6K and 3 K, respectively.

Most of other *RE* oxides, such as Ce_2O_3 and Pr_2O_3, have been reported to be paramagnetic and obey linear $1/\chi$ - *T* relationship derived from the Curie-Weiss law [7].

1.2 Previous studies of Rare Earth monoxide (*RE*O)

1.2.1 Thermodynamic stability of solid state *RE*O

Before the report by J.M. Leger *et al*. [14,15,16], synthesis of bulk *RE*O except for EuO had been attempted under ambient conditions. However, the obtained compounds were proved to be oxidenitrides [17] and the existence of *RE*O had been controversial [18,19].

Based on the calculation for standard Gibbs energy of formation, J.M. Leger *et al*. discussed the thermodynamic stabilities of *RE*O, focusing on whether solid-state *RE*O could be prepared by reduction of sesquioxide with pure metal [16]. The standard enthalpy energy change $\Delta H^{\circ}{}_1$ for the following reaction

$$RE + RE_2O_3 \rightarrow 3RE^{2+}O^{2-} \quad (1)$$
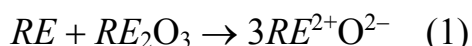
can be evaluated by the thermodynamic cycle of Fig. 1.7.

$$RE(s) \quad + \quad RE_2O_3(s) \xrightarrow{\Delta H^\circ_1} 3RE^{2+}O^{2-}(s)$$
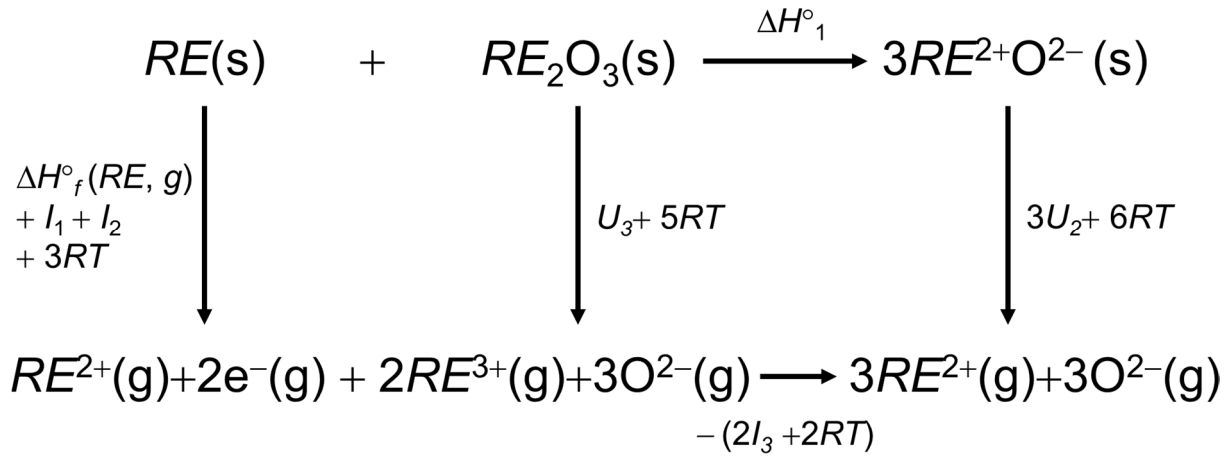
Figure 1.7 Thermodynamic cycle for the formation of a divalent REO from RE metal and RE_2O_3.

The following equation should hold,

$$\Delta H^\circ_1 = \Delta H^\circ_f(RE, g) + I_1 + I_2 + I_3 + U_3 - 3U_2 - 3I_3 \quad (1.2)$$

where $\Delta H^\circ_f(RE, g)$ is the enthalpy of atomization of the metal, U_2 and U_3 are the crystal lattice energies of REO (rocksalt) and RE_2O_3 (C-type), I_1, I_2, I_3 are the first, second, and third ionization energies of the RE element, respectively. The standard Gibbs energy change for reaction (1) ΔG°_1 is obtained from

$$\Delta G^\circ_1 = \Delta H^\circ_1 - T\Delta S^\circ_1 \quad (1.3)$$

where ΔS°_1 is the entropy change for reaction (1). In case of RE=Eu, the term $T\Delta S^\circ_1$ evaluated from available data is small (~ 7 kJ). In the lanthanide series, the term $T\Delta S^\circ_1$ is nearly constant, although small irregularities due to magnetic or crystallographic phase transitions are recognizable. Therefore, the standard Gibbs energy change for reaction (1) can be expressed as

$$\Delta G^{\circ}{}_1 = \Delta H^{\circ}{}_f(RE, g) + I_1 + I_2 + I_3 + U_3 - 3U_2 - 3I_3 - C \quad (1.4)$$

where C is a constant (+ 10 kJ).

The $\Delta G^{\circ}{}_1$ values calculated from the equation are shown in Table 1.3 and Fig. 1.8; they are positive for all REOs except for EuO and YbO, confirming the instability of REO. Meanwhile, EuO has negative $\Delta G^{\circ}{}_1$ of -141 kJ, which is consistent with the previous result (-155 ± 33 kJ [18]).

Applying pressure can reduce $\Delta G^{\circ}{}_1$ by $d(\Delta G^{\circ}{}_1) = \Delta V_1 \cdot dP$ because of negative ΔV_1 (Table 1.3), where ΔV_1 is the volume difference between REO and the reactants. However, ΔV_1 and the corresponding $P\Delta V_1$ term are too small to make ΔG_1 negative. Considering the $\Delta G^{\circ}{}_1$ and ΔG_1 values, the formation of divalent REOs, except for EuO and possibly YbO, is extremely difficult even under high pressure.

Table 1.3 Standard Gibbs energy change and volume variations for the reactions.

All data are acquired from Table 1 of [16].

|	$\Delta H^\circ_f + I_1 + I_2 + I_3$ [kJ]	U_3 [kJ]	U_2 [kJ]	$\Delta H^\circ_f + I_1 + I_2 + I_3 + U_3 - 3U_2$ [kJ]	ΔG°_1 [kJ]	ΔG° [kJ]	M [kJ]	ΔV_1 [cm^3]	ΔV [cm^3]
La	3887	12780	3362	6581	1276	3	5563	− 1.6	− 10.5
Ce	3943	12897	3379	6703	846	10	5618	~ 0	− 9.2
Pr	3985	13002	3396	6799	528	17	5675	~ 0	− 9.7
Nd	4024	13057	3414	6839	434	24	5694	− 0.9	− 10
Pm	4057	13148	3432	6909	443	32	5732	− 1.4	− 10.5
Sm	4076	13200	3450	6926	142	38	5754	− 2.6	− 10.4
Eu	4213	13275	3468	7084	−141	130	5794	− 11.8	—
Gd	4147	13320	3487	7006	1110	53	5813	− 3.6	− 10.7
Tb	4179	13409	3506	7070	718	60	5849	− 3.2	− 11.5
Dy	4188	13475	3525	7088	478	67	5873	− 4.7	− 11.6
Ho	4224	13534	3542	7132	510	74	5903	− 4.1	− 11.4
Er	4250	13596	3563	7157	565	82	5929	− 4.4	− 11.4
Tm	4276	13660	3581	7193	328	89	5957	− 4.3	− 11.2
Yb	4350	13715	3603	7256	~ 0	138	5983	− 11.7	—
Lu	4338	13757	3623	7226	1150	103	6005	− 3.7	− 11.6
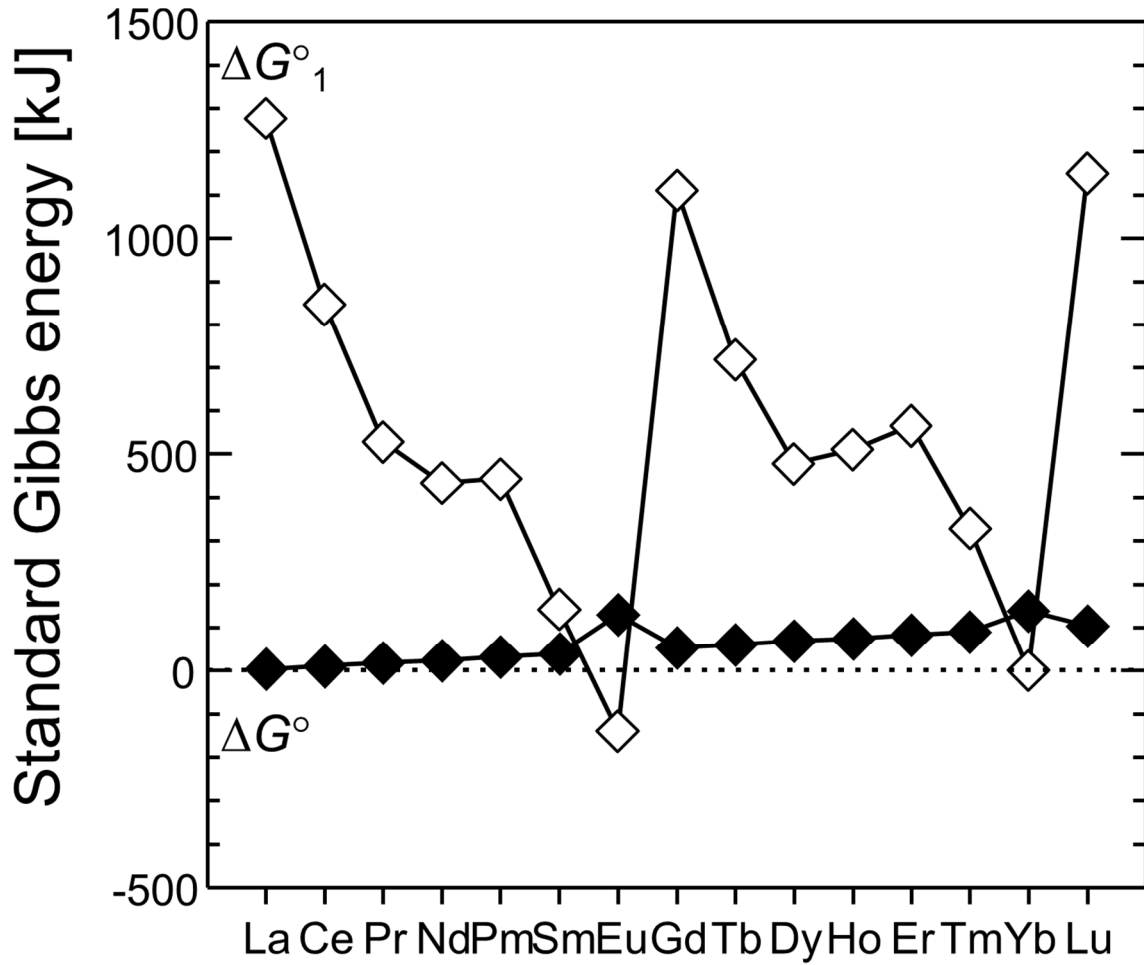
Figure 1.8 Standard Gibbs energy change $\Delta G°_1$ for the reaction $RE + RE_2O_3 \rightarrow 3\ RE^{2+}O$ and $\Delta G°$ for the reaction $RE + RE_2O_3 \rightarrow 3\ RE^{3+}(e^-)O$ [16].

On the other hand, the standard Gibbs energy changes $\Delta G°$ for the reaction $RE + RE_2O_3 \rightarrow 3RE^{3+}(e^-)O^{2-}$ were also evaluated. The $RE^{3+}(e^-)$ state means that one delocalized electron ($5d$ conduction electron) per RE atom, which leads to metallic properties, participates in the bonding and that the other two electrons per RE atom are accommodated by the anions in the ionic model. Thus, the total number of bonding electrons per RE atom is equal to 3. $\Delta G°$ is calculated from

$$\Delta G° = \Delta G°_1 + \Delta G°_2 \qquad (1.5)$$

where $\Delta G°_2$ corresponds to transformation from divalent state to trivalent state. $\Delta G°_2$ can be analyzed by the thermodynamic cycle shown in Fig. 1.9 using the following relations

$$\Delta H°_2 = 3U_2 + 3I_3 - 3M + 9RT \quad (1.6)$$

$$\Delta G°_2 = \Delta H°_2 - T\Delta S°_2 \quad (1.7)$$

where M is the dissociation energy of the trivalent REO. Under the induced pressure, $\Delta G°_2$ can also be reduced by $d(\Delta G°_2) = \Delta V_2 \cdot dP$ due to the negative ΔV_2, where ΔV_2 is the volume difference between divalent and trivalent monoxides.

$$3RE^{2+}O^{2-}(s) \xrightarrow{\Delta H°_2} 3RE^{3+}(e^-)O^{2-}(s)$$

$$\Big\downarrow 3U_2 + 6RT \qquad\qquad \Big\downarrow 3M$$

$$3RE^{2+}(g) + 3O^{2-}(g) \xrightarrow{\quad} 3RE^{3+}(g) + 3e^-(g) + 3O^{2-}(g)$$
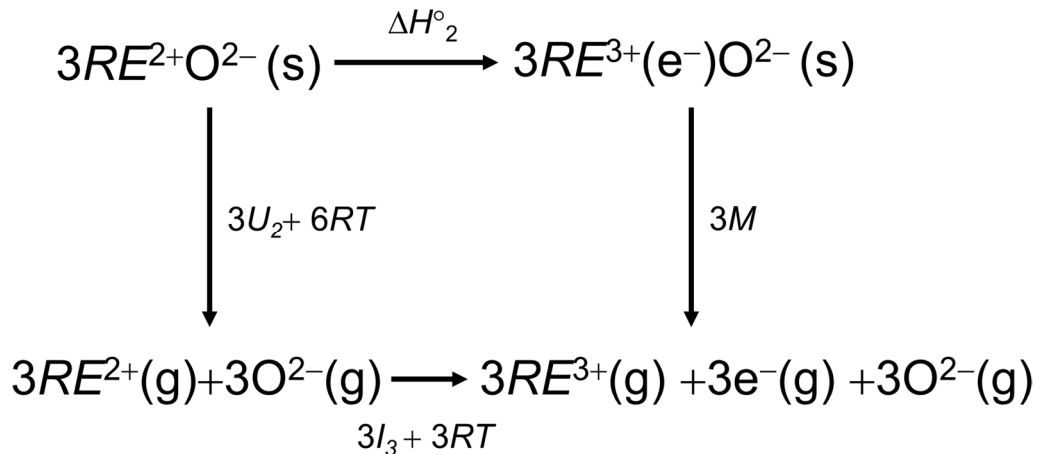
$$3I_3 + 3RT$$

Figure 1.9 Thermodynamic cycle for conversion of divalent REOs to a trivalent state.

As shown in Fig. 1.8 and Table 1.3, the $\Delta G°$ values are calculated to be positive, and there is a clear tendency that $\Delta G°$ increases with increasing the atomic number of RE element. In contrast with reaction (1), under a pressure of 50 kbar, $\Delta G°$ becomes sufficiently small because of the relatively large $\Delta V(=\Delta V_1+\Delta V_2)$, indicating a possibility for the synthesis of trivalent REO having lighter RE elements under high pressure.

In fact, as described below, J.M. Leger *et al.* performed the reactions $RE + RE_2O_3$ under high pressure to determine whether metallic (trivalent) REO could be obtained [14-16].

1.2.2 High pressure synthesis and DFT calculation

Gaseous molecules of all REOs has been observed in vapor phases by optical spectroscopy [7]. On the other hand, researches on solid-state REOs have been limited. Except for three publications by J.M. Leger *et al.* in 1980 and 1981 [14-16], there has
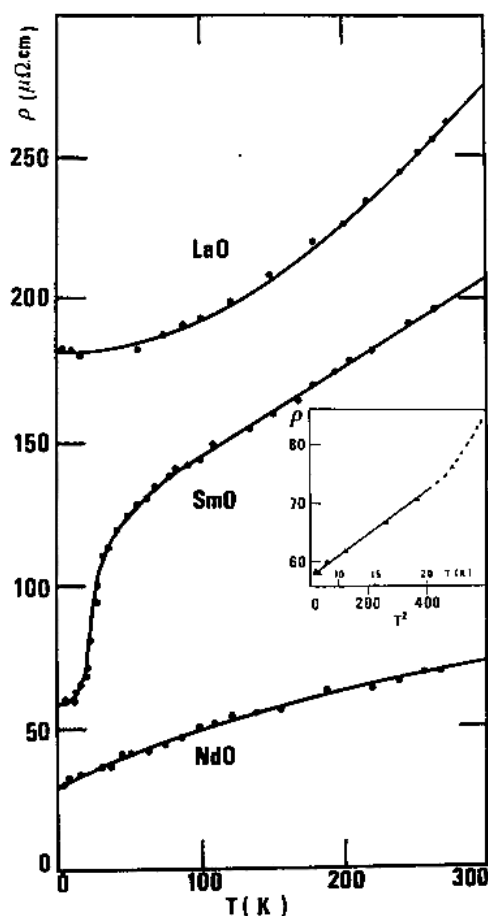

Figure 1.10 Temperature dependence of electrical resistivity of LaO, SmO and NdO. Reprinted with permission from [15]. Copyright 1980 by Elsevier.

been no report for synthesis of solid-state REO (RE = La, Ce, Pr, Nd, and Sm), possibly due to the poor chemical stability.

According to the reports by Leger et al. [14-16], REO samples were obtained from the mixed powders of RE pure metal (purity 99.9 %) and calcined RE_2O_3 (purity 99.95 %) under high pressure (10 - 80 kbar) in a compressible gasket apparatus. The reaction temperatures varied from 500 to 1200 °C. The temperature was slowly increased after the pressure was set to a desired value, and then gradually decreased after reaction time of 4 hours. The optimized pressure and temperature for each system were as follows: 40 kbar and 900 °C for LaO, 50 kbar and 800 °C for PrO, 50 kbar and 1000 °C for NdO, over 50 kbar and 1000 °C for SmO.

The high-pressure synthesis provided golden yellow bulk polycrystals of REO (RE = La, Ce, Pr, Nd, and Sm) compounds. These REO compounds contained small amounts of impurities of H < 3 at.%, C ~ 1 at.%, N ~ 0.2 at.% and showed metallic properties with room temperature resistivity of $e.g.$ 270 $\mu\Omega$.cm in LaO, as shown in Fig. 1.10 [15].

The crystal structures were analyzed to be face-centered cubic structure with lattice constants of 5.144, 5.089, 5.031, 4.994, and 4.943 Å, ($\pm$ 0.005 Å), respectively. The lattice constants of LaO, CeO, PrO and NdO were reasonable considering from the ionic radii of RE^{3+}. On the other hand, SmO was evaluated to have an intermediated valence state of $Sm^{2.9+}$ from Vegard's law. As shown in Fig. 1.11(a), PrO and NdO exhibited paramagnetic properties with paramagnetic Curie temperatures of -40 K and -36 K, respectively. As shown in Fig. 1.11(b), SmO showed temperature independent Van Vleck susceptibility ($\sim 6 \times 10^{-3}$ emu/mole).
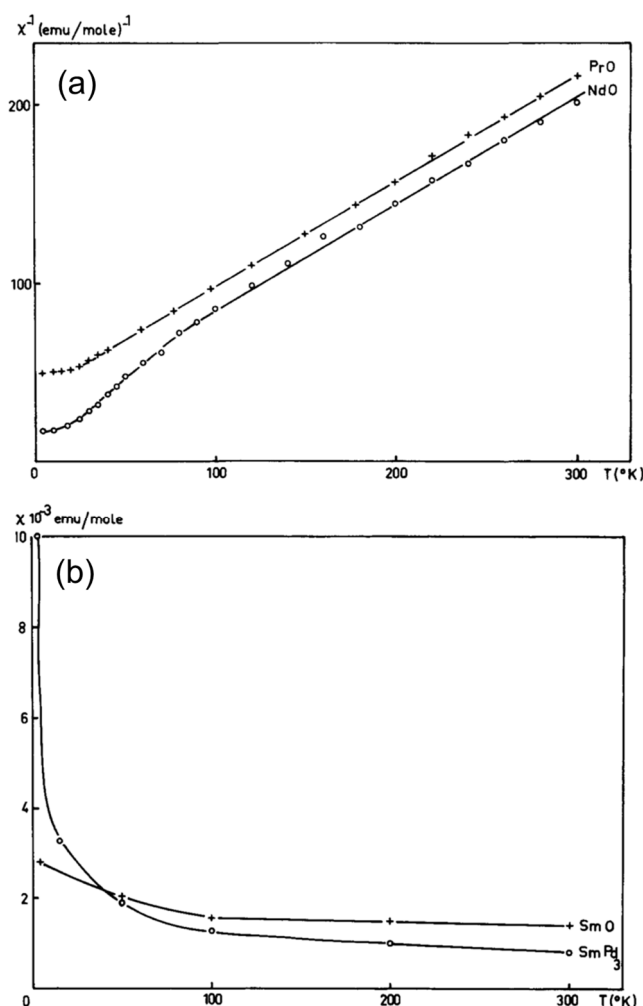

Figure 1.11 Temperature dependence of (a) inverse magnetic susceptibility of PrO, NdO and (b) magnetic susceptibility of SmO. Reprinted with permission from [14]. Copyright 1980 by Elsevier.

The similar reactions were also conducted for *RE* = Gd, Dy, and Tm at 50 kbar and 1000 °C, however *RE*O could not be synthesized possibly due to the large positive values of $\Delta G°$ [16].

Recently, total and partial densities of states (DOS) for *Ln*O (*Ln* = La, Ce, Pr, Nd, Sm, Eu, Tb, Ho, Er and Yb) were calculated using density functional theory (DFT), as shown in Fig. 1.12 [20]. According to the results, all *Ln*Os shows metallic properties without gap opening and at part of DOS derived from *Ln* elements mainly crosses the
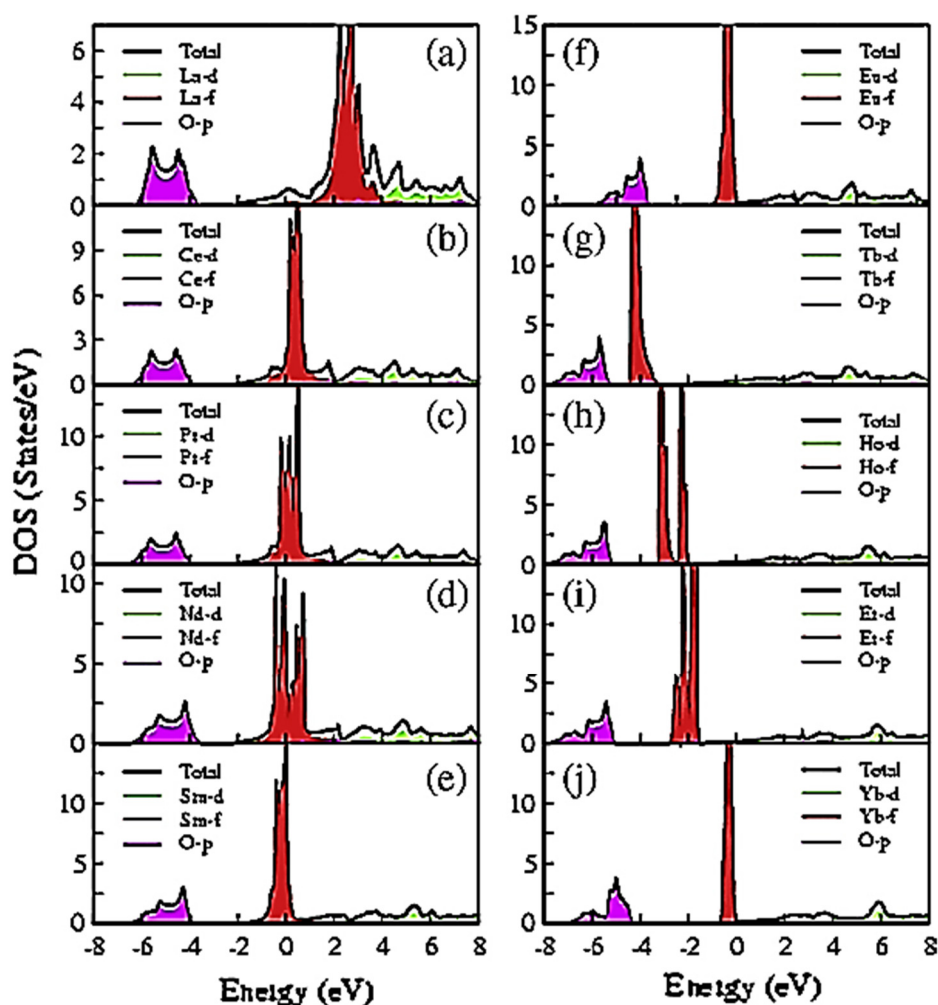

Figure 1.12 The total and partial DOS of (a) LaO, (b) CeO, (c) PrO, (d) NdO, (e) SmO, (f) EuO, (g) TbO, (h) HoO, (i) ErO, and (j) YbO. Reprinted with permission from [20]. Copyright 2015 by Elsevier.

Fermi level. The oxygen $2p$ state has lower energy than the f and d states of Ln and is more localized, whereas the f states closer to the Fermi level have more itinerant characters.

1.2.3 Ferromagnetic semiconductor: EuO

EuO is a well-established ferromagnetic semiconductor with a bandgap of 1.12 eV between the half-filled Eu $4f$ band and the Eu $5d$ conduction band [21,22,23,24]. The Curie temperature (T_C) of stoichiometric EuO is ~ 69 K and the divalent Eu ions with localized $4f^7$ spins carry a large magnetic moment of 7 μ_B. In recent years, the electrical and magnetic properties of EuO have attracted much attention as a potential material for spintronics devices, such as a tunnel-junction-type spin filter using EuO with spin polarization exceeding 90 % [25]. Furthermore, EuO shows colossal magnetoresistance and metal to insulator transition with a resistivity change by 8 to 13 orders of magnitude induced by electron carrier doping [26,27].

The ferromagnetism of EuO originates from the indirect exchange J_1 governed by the Eu $4f$ and $5d$ orbitals (RKKY interaction) and the superexchange J_2 involving the hybridized Eu $4f$ and O $2p$ orbitals mediated by $6s$ and $5d$ states [28,29]. T_c can be enhanced by reducing the gap between the Eu $4f$ and $5d$ states and by minimizing the hybridization between the Eu $4f$ and O $2p$ states. In fact, doping of La, Lu, or Gd was reported to enhance T_c up to approximately 200 K at maximum [30,31,32], and this phenomenon was explained by modification of the on-site and RKKY interactions [33]. T_c can also be enhanced by introducing oxygen vacancies into stoichiometric EuO [34] and by applying tensile strain to epitaxial thin film samples [35].

Recently, fabrication of high-quality EuO epitaxial thin films has been accomplished with the aid of rapid advancing thin film growth technology [36], such as pulsed laser deposition method and molecular beam epitaxy method. High-quality EuO epitaxial thin films exhibit fascinating physical properties. For example, anomalous Hall effect, presenting the Hall effect due to internal magnetic field, was observed for the first time in thin film specimens [37]. Topological Hall effect originating from noncoplanar spin configuration of two-dimensional skyrmions was also reported (Fig. 1.13) [38]. Thus, epitaxial thin film growth is suitable for investigating intrinsic and fundamental physical properties of novel compounds such as *RE*O.
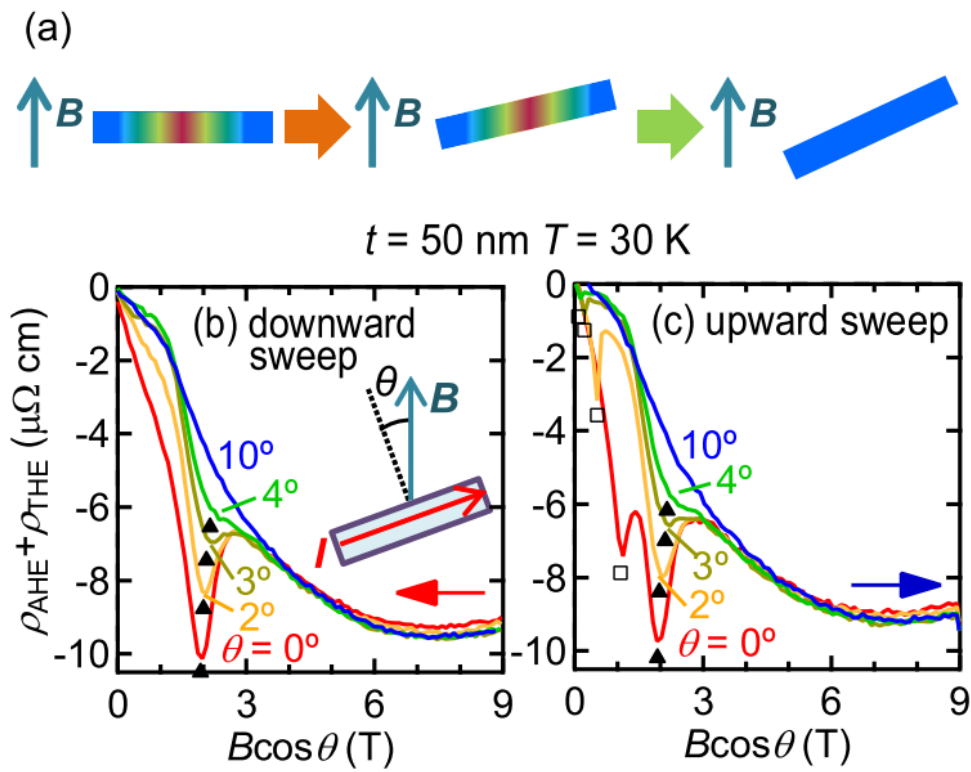

Figure 1.13 (a) Schematic images of a 2D magnetic structure in a film under inclined external magnetic field. Spin configuration (anti)parallel to magnetic field B indicates red (blue). The sum of anomalous and topological Hall resistivities ($\rho_{AHE} + \rho_{THE}$) as a function of $B\cos\theta$ for (b) downward and (c) upward sweeps of B. Reprinted with permission from [38]. Copyright 2015 by American Physical Society.

1.3 Purpose of this study

As mentioned in the previous sections, systematic research on solid-state *RE*O has been scarcely conducted so far, possibly due to the poor chemical stability. In contrast with relatively stable EuO, which has been well studied as a ferromagnetic semiconductor, bulk polycrystalline *Ln*Os (*Ln* = La, Ce, Pr, Nd, and Sm), first synthesized in 1981, showed less fascinating physical properties. After 1981, no follow-up studies have been made for solid-state *RE*O and their intrinsic properties have remained veiled for over 30 years.

Purpose of this study is to establish a process to grow high-quality *RE*O thin films by making full use of a state-of-art thin film growth technique, pulsed laser deposition (PLD) method, and to investigate their intrinsic properties. PLD is a non-equilibrium process and thus is a powerful tool to synthesize metastable materials in form of epitaxial thin films. With PLD method, I succeeded in synthesizing epitaxial thin films of YO and GdO, for the first time, which have been known only as molecular species in gaseous phases. In addition, I grew high quality LaO epitaxial thin films with crystal quality comparable to EuO. These three *RE*Os exhibited unexpected and fascinating properties, such as superconductivity and room temperature ferromagnetism. In this study, I discuss the intrinsic physical properties of these three *RE*Os in a systematic manner, with a particular focus on the electronic structures of divalent *RE*.

Chapter 2:
Experimental techniques

2.1 Pulsed Laser Deposition (PLD) method

Pulsed Laser Deposition (PLD) method is one of physical vapor deposition techniques and widely used for thin film fabrication [39]. As one of the merits, PLD is a non-equilibrium process and therefore it is suitable to synthesize metastable materials such as solid-state REO.

PLD method is schematically illustrate in Fig. 2.1(a). Inside an ultra-high vacuum chamber, of which base pressure is below ~ 10^{-10} Torr, a high power KrF pulsed laser beam ($\lambda = 248$ nm) was focused on a pellet of RE oxide (RE_2O_3) or RE metal as a target, and the instantly sublimated species are deposited onto a single crystalline substrate. The substrate temperature, monitored with a radiation thermometer, can be controlled with an infrared semiconductor laser up to ~ 1200°C. Oxygen partial pressure inside the chamber was tuned by introduction of pure O_2 gas or Ar O_2 1% mixed gas, and it was checked with a quadrupole mass spectrometer. In a relatively oxidizing atmosphere depending on the experimental conditions, such as laser frequency, laser energy, and oxygen partial pressure, the sublimated species are oxidized before reaching to the substrate. The adhered species are kinetically rearranged under an epitaxial strain from the single crystalline substrate, and finally forms an epitaxial thin film (Fig. 2.1(b)). During film fabrication, the growth morphology was monitored *in-situ* with the Reflection High Energy Electron Diffraction (RHEED) system. The observed RHEED

pattern changes with the surface structures; a single crystalline film gives a clear streak or dot-like pattern whereas an amorphous film a halo pattern.
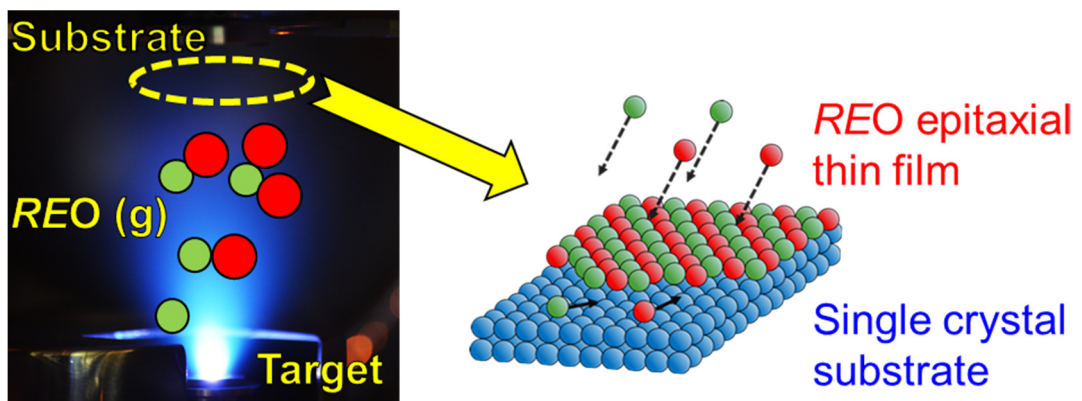
(a)
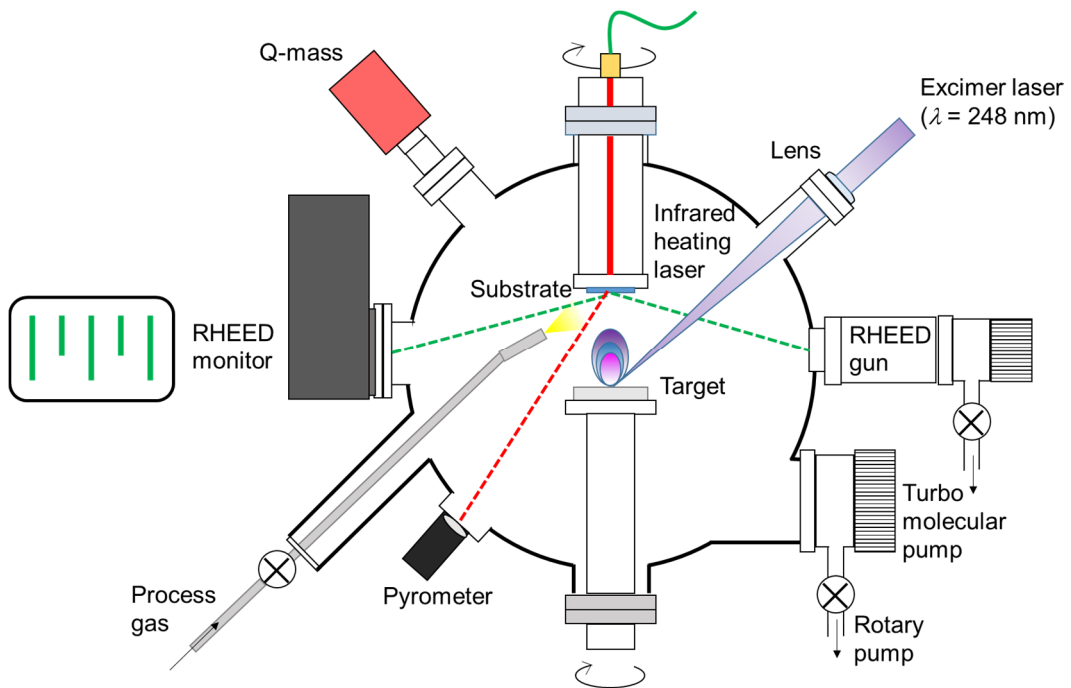
(b)

Figure 2.1 (a) A schematic image of PLD equipment. (b) A photo of plume from target and a schematic image of epitaxial growth.

In this study, PLD equipment (LC-LMBE, Pascal) was used for synthesis of solid-state YO, LaO, and GdO in epitaxial thin film form. The following experimental parameters were taken into account for PLD growth of REO epitaxial thin films.

➢ Target (RE_2O_3/ RE metal)

➢ Substrate (CaF$_2$/ oxide substrate)

➢ Introducing gas species (No gas/ pure O$_2$ gas/ Ar-1% O$_2$ mixed gas)

➢ Substrate temperature

➢ Oxygen partial pressure

➢ Laser frequency

➢ Laser energy

The optimal condition largely differed from a target material to another, due to the difference in reactivity with oxygen, and thus it needs to be determined, independently.

2.2 Crystal structure analysis

2.2.1 X-ray diffraction (XRD)

X-ray diffraction (XRD) is a measurement method generally used for crystal structure analysis [40]. As shown in Fig. 2.2, let us consider a case where X-rays of wavelength λ incident at an angle θ on a lattice plane of a crystal lattice. On this occasion, when the relation

$$2d \sin\theta = n\lambda \quad (2.1)$$

holds, the X-rays reflected by the two parallel lattice planes with a lattice spacing d interfere with each other, and the diffraction intensity of the X-rays is enhanced. This equation is called as Bragg's law, and X-ray diffraction is observed when the geometrical relation satisfies this condition and d can be calculated from θ.
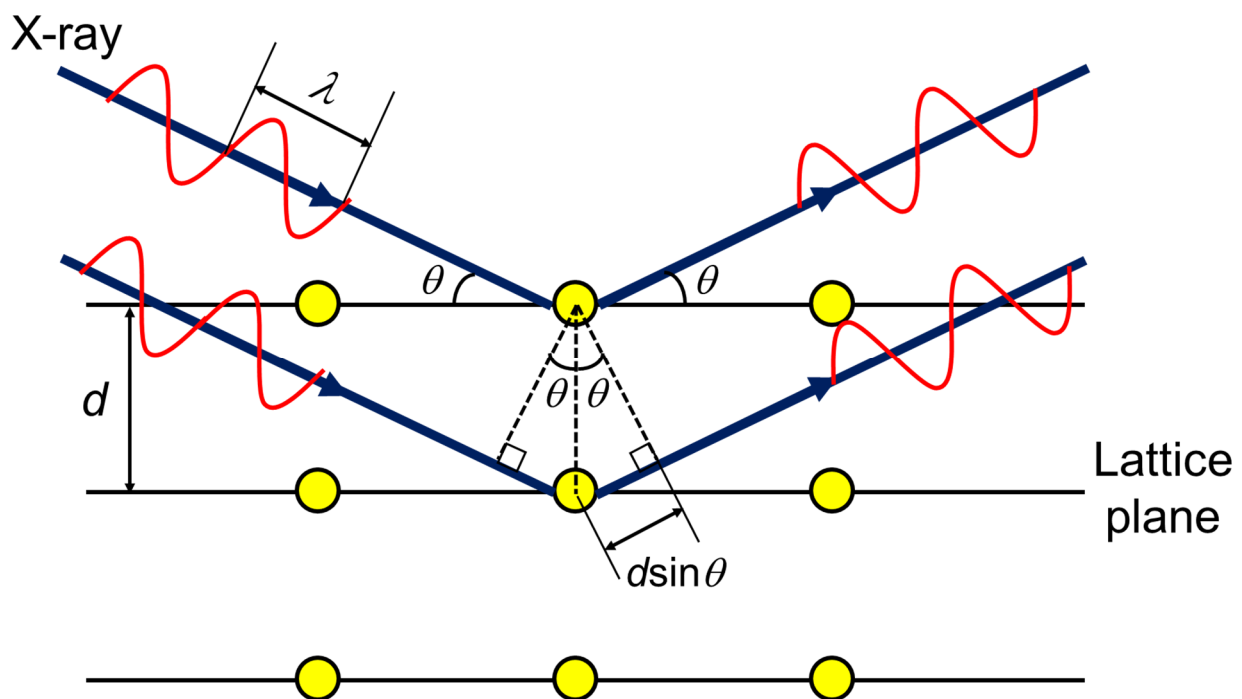

Figure 2.2 A schematic image of Bragg's law.

X-rays are scattered by electrons spreading around atoms. Therefore, the amplitude of diffracted X-rays can be expressed using structural factors approximated by the sum of the electron densities of all the atoms in the unit lattice. The crystal structure of a sample can be analyzed by determining lattice constants and structural factors from the measured XRD diffraction angle and intensity ($\propto$ squared amplitude).

In case of thin films, crystallinity and crystal orientation can be evaluated by XRD. From 2θ-ω scans ($\omega = \theta$) on thin film samples (Fig. 2.3), only the diffraction peaks from the lattice planes parallel to the surface of the thin film, satisfying the Bragg diffraction condition, are observed. Therefore, if the thin film is of epitaxial thin film form, only the diffraction peak of a specific orientation surface is observed, and, in other words, surface orientation can be determined from the result of the 2θ-ω scan. For example, ifs the thin film is c-axis oriented (when the c-axis <001> is perpendicular to the thin film surface), only the diffraction peaks of $(00l)$ plane can be observed.

Measurement of diffraction intensity changing only ω at fixed 2θ is called rocking curve measurement. When rocking curve measurement is performed on the diffraction peak of the $(00l)$ plane of a c-axis oriented thin film, the width of the diffraction peak is proportional to the degree of fluctuation of c-axis length (mosaicity).
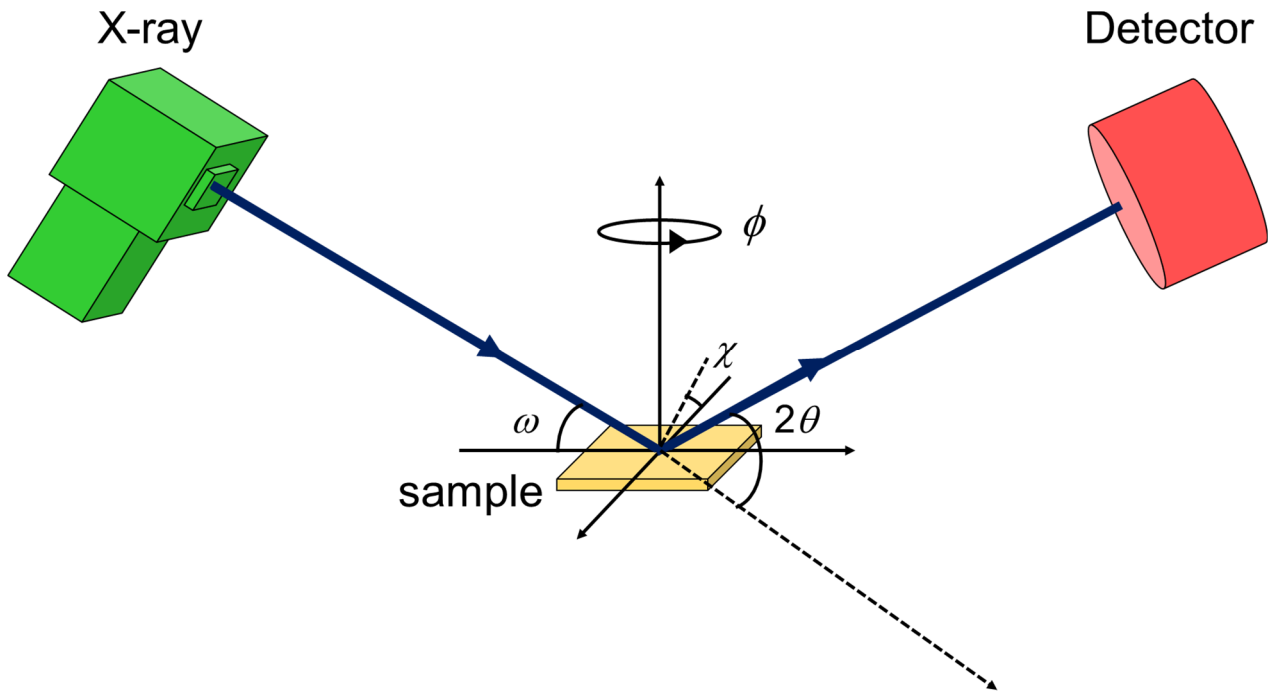
Figure 2.3 A schematic image of 4-axis X-ray diffractometer (2θ, ω, ϕ, χ).

In-plane orientation can be investigated by performing ϕ scan on a thin film whose orientation in the perpendicular direction has already been identified from 2θ-ω scan. In ϕ scan measurement, a thin film sample is tilted in the χ direction and then rotated in the in-plane direction (ϕ direction) so that diffraction from lattice planes which is not parallel to the film surface can be measured. For example, in case of an epitaxial thin film in which crystal lattice is well aligned even in the in-plane direction, a diffraction peak is observed at an angle χ representing the symmetry of the crystal. One can repeat this ϕ scan while changing χ little by little, which is called pole measurement, and the obtained result is called pole figure.

A measurement method called Reciprocal Space Mapping (RSM) is a method for investigating lattice distortion of thin film samples from the relationship between the reciprocal lattices of film and substrate. RSM measurement can also be conducted for the diffraction from a lattice plane which is not parallel to the film surface, similar to ϕ

scan. In this case, the thin film sample is tilted in χ direction, and multiple 2θ-ω scans are performed while gradually changing ω. RSM image is obtained by plotting the diffraction intensity against $Q_{//} = 1/\lambda\,[\cos\omega - \cos(2\theta - \omega)]$ and $Q_{\perp} = 1/\lambda\,[\sin\omega + \sin(2\theta - \omega)]$ from the data obtained by the RSM measurement (Fig. 2.4), where $Q_{//}$ and $Q_{\perp}$ denote the reciprocal lattice space coordinates in the in-plane and out-of-plane directions. If the diffraction peaks of thin film and substrate appear at the same $Q_{//}$ position, it means that the film has the same in-plane lattice constants as the substrate, representing epitaxial growth of the thin film [41].

In this study, crystal structure analysis of *RE*O epitaxial thin films was performed using D8 DISCOVER (Bruker AXS) X-ray diffractometer.
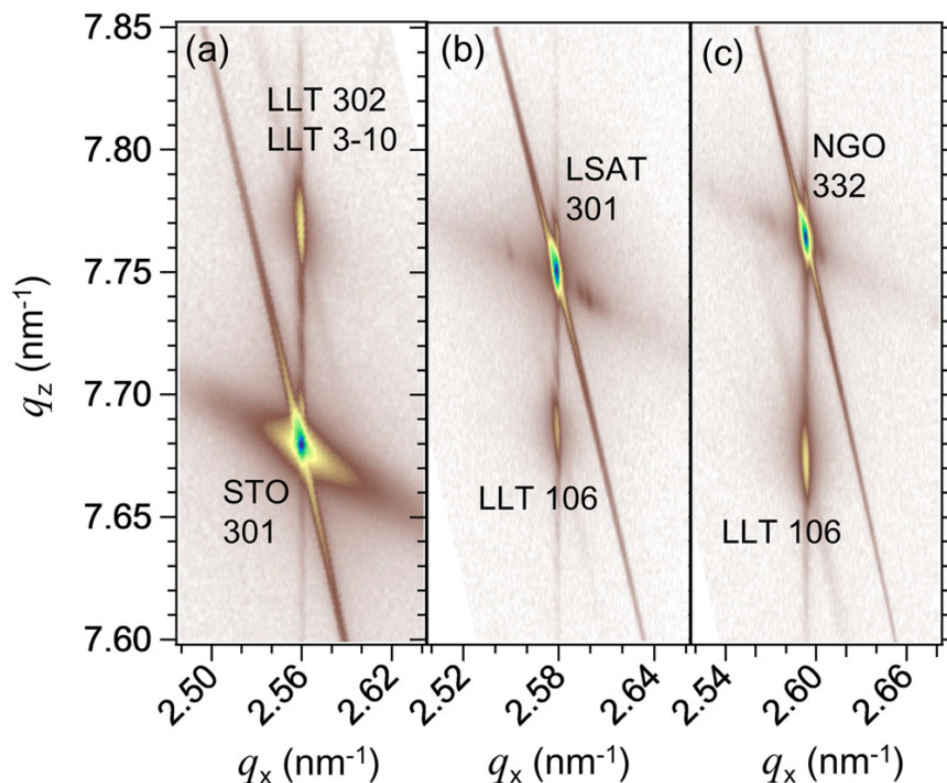

Figure 2.4 An example of RSM image. Reciprocal space mappings of $Li_{0.33}La_{0.56}TiO_3$ (LLT) thin films with epitaxial strain on (a) $SrTiO_3$ (100), (b) LSAT (100), and (c) $NdGaO_3$ (110). Reprinted with permission from [41]. Copyright 2015 by American Chemical Society.

2.2.2 Transmission Electron Microscope (TEM)

Transmission Electron Microscope (TEM) is an electron microscopic technique in which electrons transmitted through a specimen are observed to obtain magnified images [42], as schematically illustrated in Fig. 2.5.

TEM visualizes the difference in transmittance of electron beam, which depends on the surface or internal structure of the sample. In addition, since the irradiated electron beam needs to pass through the sample, it is necessary to prepare a thin sample with a thickness of 100 nm or less.

Electron
gun

Condenser
lens

Specimen $\updownarrow$ < 100 nm
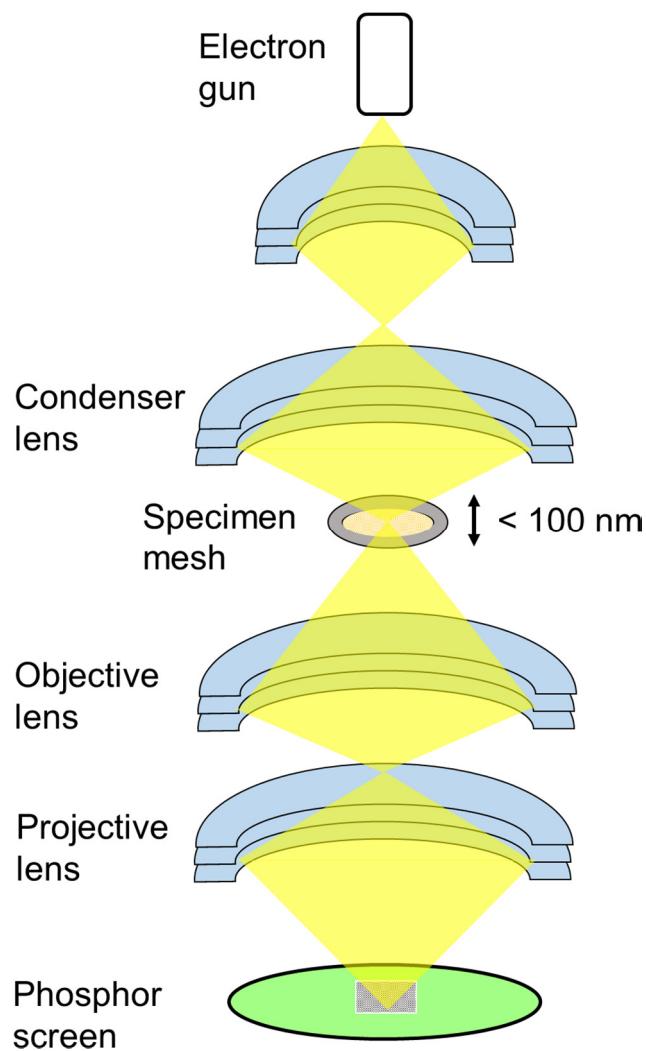mesh

Objective
lens

Projective
lens

Phosphor
screen

Figure 2.5 A schematic image of TEM measurement.

In this study, TEM measurement (JEM-2100(HR), JEOL) was performed with support from Technical Division, School of Engineering, Tohoku University to analyze the crystal structure of solid-state YO.

2.2.3 Atomic Force Microscopy (AFM)

Atomic Force Microscope (AFM) is a type of microscope that detects interatomic forces acting between probe and sample [43], as shown in Fig. 2.6.

An AFM probe attached to the end of a cantilever is brought into contact with sample surface with a small force. By scanning the probe in the horizontal (X, Y) directions, keeping the probe-sample distance (Z) constant, surface topographic images can be obtained. The deflection of the cantilever is detected by an optical lever system, where
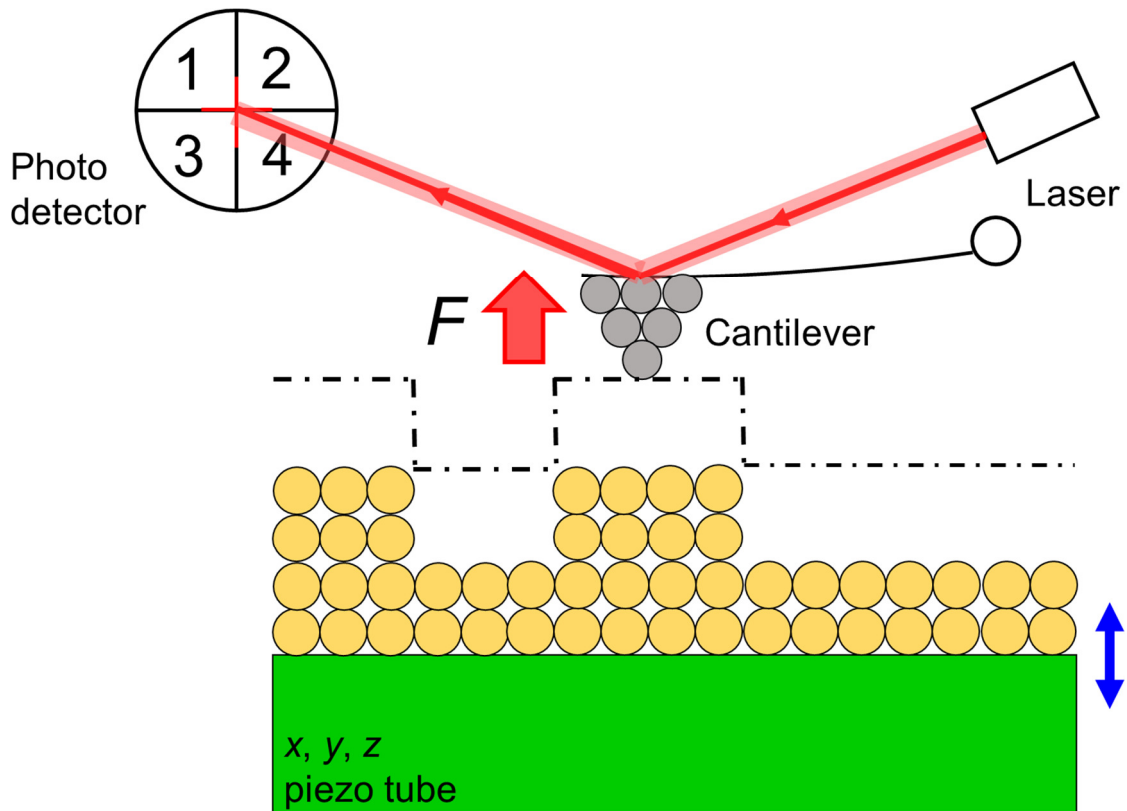
Figure 2.6 A schematic image of AFM measurement.

a laser beam reflected at the back of the cantilever is detected by four position sensors which sense up/ down and left/right displacement of the beam.

In this study, AFM equipment (E-sweep, Hitachi Nanotechnology Science) was used to confirm step and terrace structures of annealed oxide substrates.

2.3 Electronic structure analysis and composition analysis

2.3.1 X-ray Photoemission Spectroscopy (XPS)

When a sample surface is irradiated with X-rays, electrons in the sample (solid) absorb the photons and are excited to a vacuum level, i.e., electrons are released from the sample surface [44]. By measuring the kinetic energy distribution of the released electrons, information about the electronic state in the sample can be obtained, as shown in Fig. 2.7. Such a measurement is called X-ray Photoelectron Spectroscopy (XPS). Due to the conservation of energy, the following relationship holds,

$$E_k = h\nu - E_B - \phi \quad (2.2)$$

where E_k is the kinetic energy of photoelectron, $h\nu$ is the energy of irradiated photon, E_B is the binding energy of electrons in the sample relative to E_F and ϕ is the work function. Using this relationship, the measured photoelectron spectrum as a function of E_k can be transformed into the density of states as a function of E_B below E_F.

Oxidation states can be examined by XPS. The binding energy of the inner shell level shifts, depending on the valence state and the coordination state (bonding state) of element, which is referred to as chemical shift. If the relationship between valence state and chemical shift is already known for reference materials, the valence or chemical state of the sample can be estimated from the chemical shift.
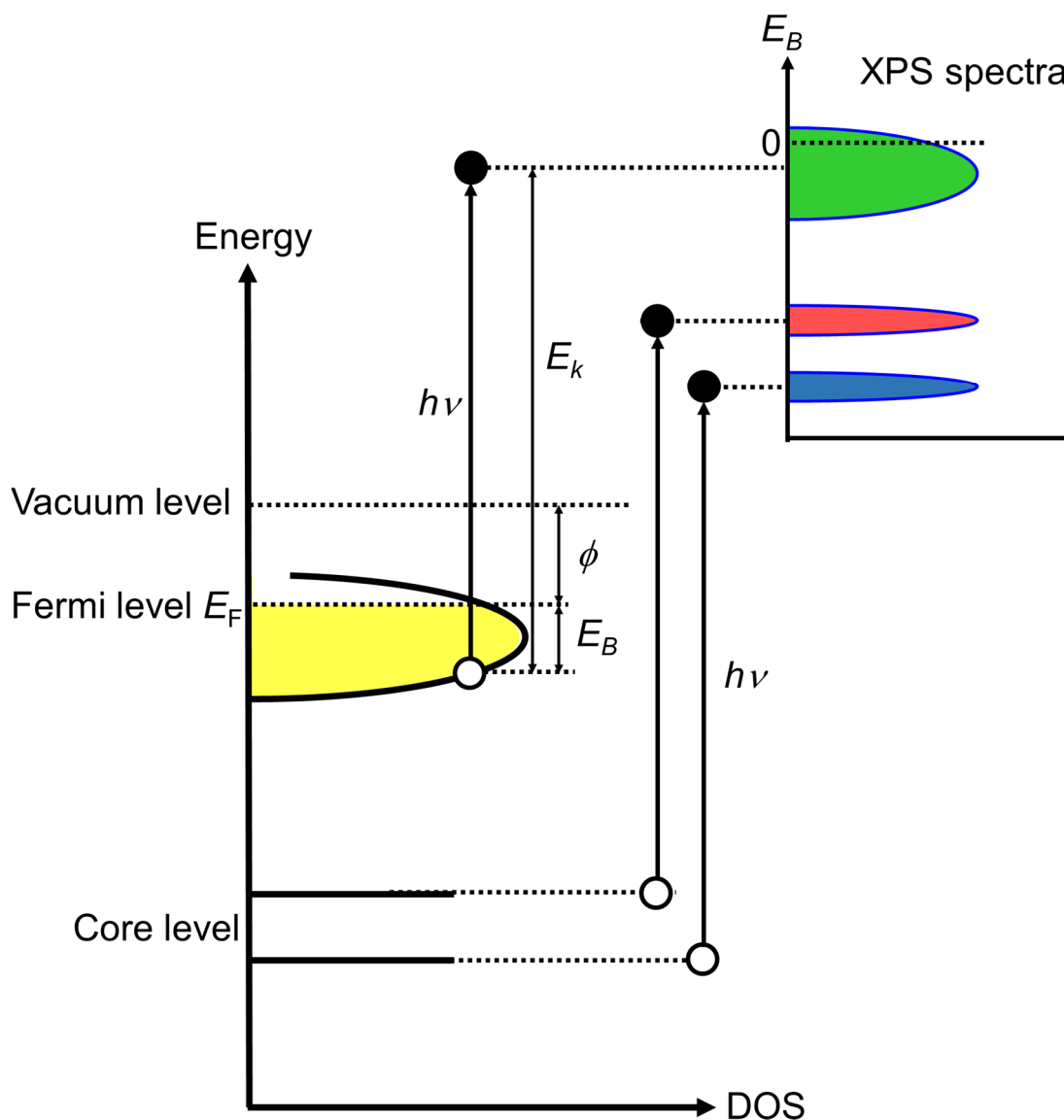

Figure 2.7 A schematic image of XPS measurement.

Furthermore, quantitative composition analysis can be performed from the peak intensities of constituent elements. In this study, for the quantitative analysis, MultiPak (Ulvac-Phi Inc.) was used as an analysis software. The penetration depth of XPS was

about 3 nm. Thus, when measuring the inside of the sample, the sample surface was etched with an accelerated Ar ion beam. In this process, composition distribution in the depth direction also can be measured.

In XPS measurements, electrons having a negative charge are extracted from the sample surface, and therefore the sample becomes positively charged unless electrons are supplied from outside. For this reason, in this study, electrons emitted from the sample were supplemented by a neutralizing electron gun attached to the XPS apparatus, and the potential distribution on the surface was kept constant. The peak of C1s originating from surface contaminated hydrocarbon (284.8 eV) was used to correct for the charging effect [45].

In this study, XPS measurements (PHI 5000 VersaProbe, Ulvac-Phi Inc.) using Al $K\alpha$ radiation (1486.6 eV) were conducted at Research Hub for Advanced Nano Characterization, The University of Tokyo, under the support of Nanotechnology Platform by MEXT, Japan (No. 12024046)..

2.3.2 Observation of X-ray Absorption Near Edge Structure (XANES)

When X-ray is irradiated on a substance, a part of X-ray is absorbed. The amount of X-ray absorption abruptly increases when the energy of X-ray exceeds a value characteristic of each element. This energy is called X-ray absorption edge. Near the X-ray absorption edge, a fine structure is observed, which is called X-ray Absorption Fine Structure (XAFS). XAFS is divided into two regimes, X-ray Absorption Near Edge Structure (XANES) located at −50 to +50 eV from the absorption edge and Extended X-ray Absorption Fine Structure (EXAFS) away from the absorption edge (about +50 to +1500 eV) (Fig. 2.8) [46].

In XANES, electrons in the inner shell are excited to unoccupied levels or quasi-continuous bands. The excited electrons are transferred to the orbitals with complicated structures, and a fine structure appears near the absorption edge. Therefore, the XANES spectrum is sensitive to the symmetry of coordination, and in case of cation the absorption edge appears at higher energy as the valence number is large. From the qualitative comparison of XANES spectra between reference and sample, it is possible to determine the valence state of the absorbed element and the 3D coordination environment.
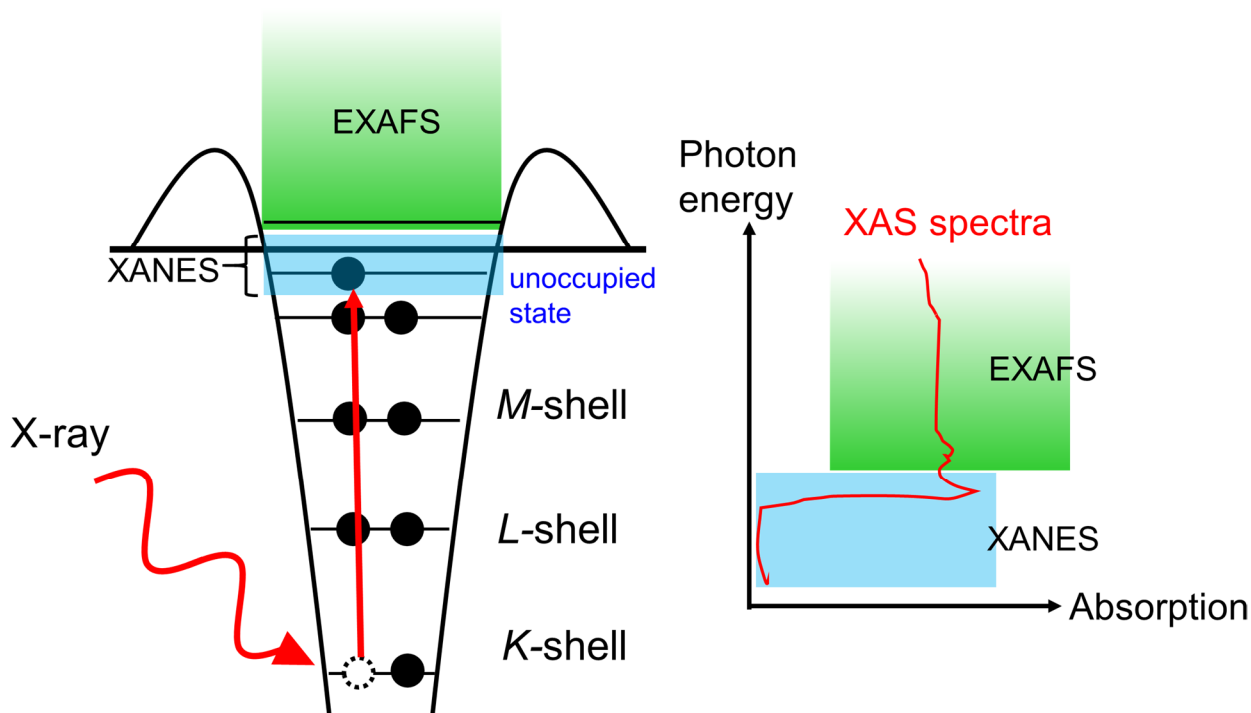

Figure 2.8 A schematic image of XAS measurement.

In this study, XANES measurements were performed at BL13XU, SPring-8 (Proposal No. 2015A0116) to analyze the valence state of Y ion in solid-state YO.

2.4 Electrical transport measurement

In this study, Physical Properties Measurement System (PPMS) manufactured by Quantum Design Co., Ltd. was used for electrical transport measurements. The set-up of this instrument is almost the same as MPMS, as described later, and it enables automatic measurements in a wide temperature range below room temperature (≥ 1.85 K) under external magnetic field up to 9 T.

2.4.1 Four-probe method

To avoid the influence of contact resistance between thin film and electrodes, resistivity was evaluated using four-probe method, as shown in Fig. 2.9(a) [47]. The four probes consist of the two probes for taking a current path (I) and the other two for reading the voltage drop (V_1, V_2). The measured area is marked by a red rectangle in Fig.2.9(a). Since almost no current flows in the latter path for measuring the voltage, the voltage drop due to the contact resistance can be neglected, which allows resistivity measurements free from the influence of contact resistance.

Hall-bar shaped thin films as shown in Fig. 2.9(a) were fabricated using a metal shadow mask for transport measurements. An alloy of indium and tin was used as electrodes for soldering wires. Voltage measurement terminals were made at two places, V_1 and V_2, to check the uniformity of the sample. Resistivity ρ was determined from the measured data (V_1, V_2, I) and film thickness t measured with a step profiler, using the following equation.

$$\rho = \frac{V_1 + V_2}{2I} \cdot t \cdot \frac{1.0 \text{ mm}}{2.4 \text{ mm}} \quad [\Omega.\text{cm}] \quad (2.3)$$

In addition, magnetoresistance was measured by sweeping magnetic field from 9 T to − 9 T at 8 different temperatures of 2, 5, 10, 20, 50, 100, 200, and 300 K. Magnetic field was applied perpendicular to the sample surface. The measured resistivity was normalized by dividing it (ρ[T]) by the resistivity at 0 T (ρ[0]). By using a sample rotator, the direction of applied magnetic field was changed from in-plane (parallel to film surface) and out-of-plane (perpendicular to film surface) direction
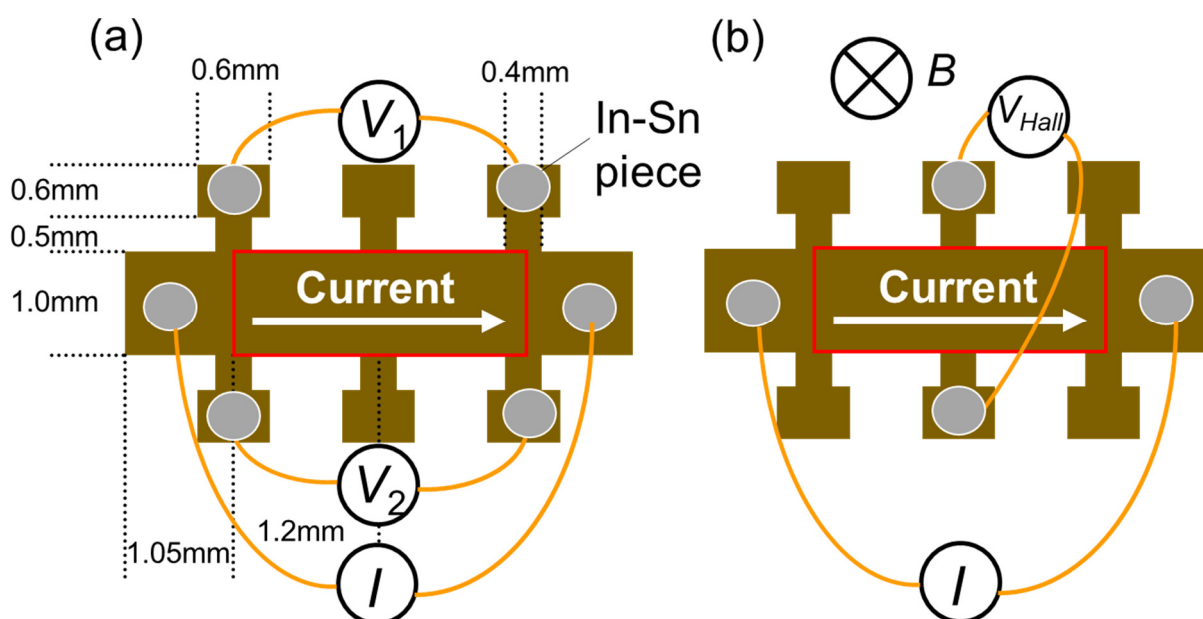

Figure 2.9 A schematic image of resistivity measurement with a Hall-bar shaped sample. (a) four-probe measurement and (b) Hall measurement.

2.4.2 Hall measurement

To determine carrier density and carrier mobility, Hall resistance ($R_{Hall} = V_{Hall}/I$) was measured simultaneously with the magnetoresistance, where voltage was recorded across the sample, as shown in Fig. 2.9(b). Ideally, Hall voltage is proportional to magnetic field H but, in actual measurements, an even component is superimposed on the Hall resistance being an odd function. Therefore, the even component was removed

by the operation of $(V_{Hall}[H] - V_{Hall}[-H])/2$, and only the linear component was extracted from the measured data.

Hall coefficient (R_H), carrier density (n) and carrier mobility (μ) are calculated from the following equations,

$$R_H = \frac{dR_{Hall}}{dB} t \quad [m^3/C] \quad (2.4)$$

$$n = \left| \frac{1}{R_H e} \right| \quad [cm^{-3}] \quad (2.5)$$

$$\mu = \left| \frac{R_H}{\rho} \right| \quad [cm^2/V.s] \quad (2.6)$$

where e (= 1.602176×10^{-19} [C]) is the elementary charge. From the sign of R_H, the carrier type, n-type (negative) or p-type (positive), can be determined.

2.5 Magnetic measurement

In this study, Magnetic Properties Measurement System (MPMS) manufactured by Quantum Design Co., Ltd. was used to evaluate the magnetic properties of *RE*O epitaxial thin films.

This instrument is mainly composed of two parts, a sample chamber that stores liquid He and liquid N_2 and is equipped with a superconducting magnet (5 T), and an external control unit. Measurement temperature can be lowered down to 1.8 K, and automatic measurements can be performed by assembling sequences by the external control system. Magnetization is quantitatively measured by a superconducting quantum interference device (SQUID) [48]. SQUID is a superconducting ring with two insulating gaps (Josephson junction) (Fig. 2.10). When the magnitude of the magnetic flux penetrating the ring changes, current flows in the ring due to the Josephson effect. By

detecting this voltage, very high sensitivity magnetization measurement can be performed.
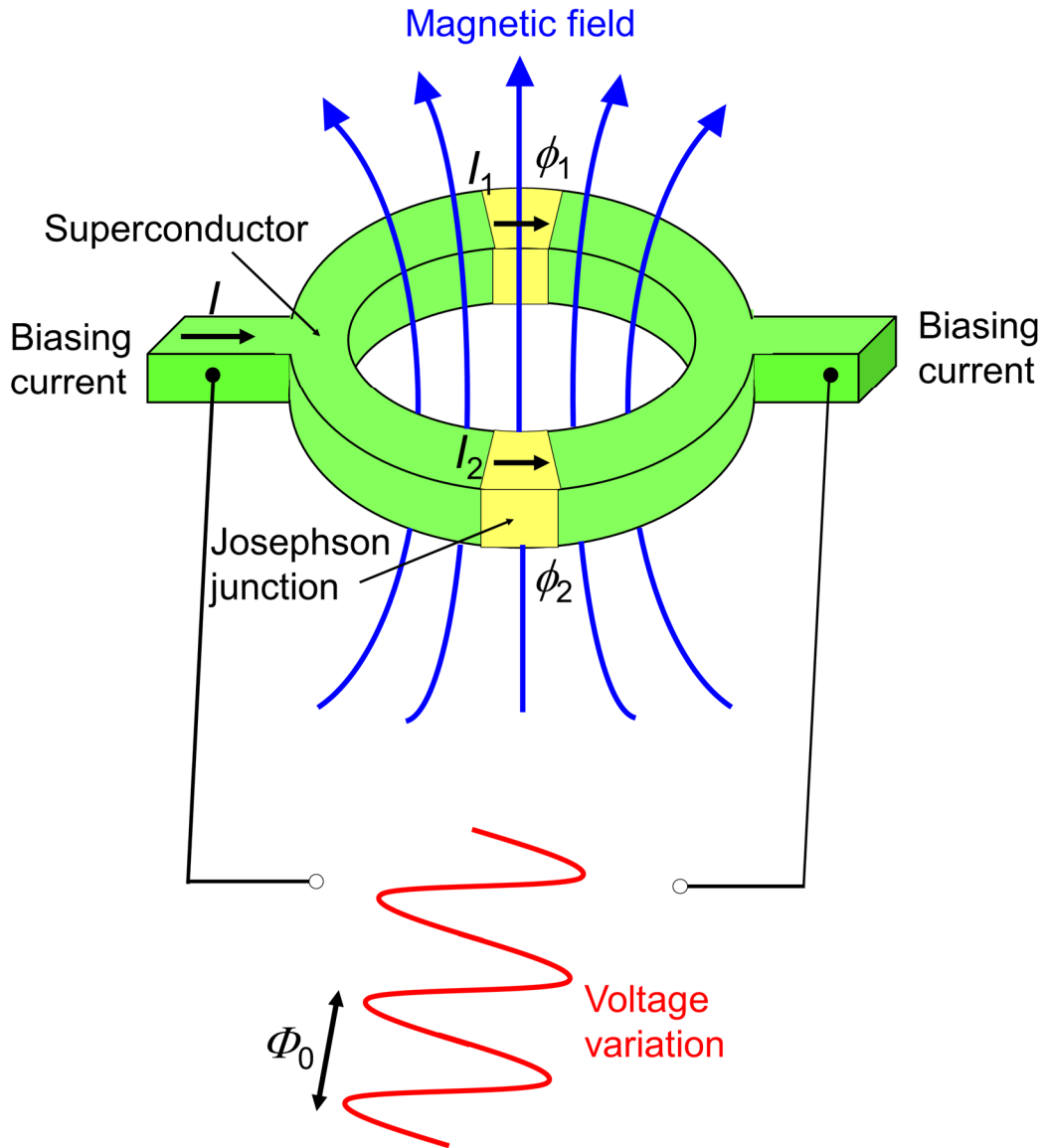

Figure 2.10 A schematic image of SQUID.

2.5.1 SQUID

In SQUID, an interference pattern appears in response to the magnetic field penetrating the superconducting ring, not at the junction. The total magnetic flux inside the

superconducting ring, $\Phi (= HA$; H: applied magnetic field, A: area of the ring), is related to the phase differences at Josephson junctions 1 and 2, ϕ_1 and ϕ_2, respectively, as,

$$\phi_1 - \phi_2 = \frac{2\pi\Phi}{\Phi_0} \quad (2.7)$$

where Φ_0 is the magnetic flux quantum.

The total current I flowing through the SQUID is the sum of the currents flowing through the Josephson junctions 1 and 2, I_1 and I_2, respectively, and is given by,

$$I = I_1 + I_2 = I_{C1}\sin\phi_1 + I_{C2}\sin\phi_2$$

$$= I_{C1}\sin\phi_1 + I_{C2}\sin\left(\phi_1 - \frac{2\pi\Phi}{\Phi_0}\right) \quad (2.8)$$

where I_{C1} and I_{C2} are the critical currents of Josephson junctions 1 and 2, respectively.

Here, if the critical currents of the two Josephson junctions are the same ($I_C = I_{C1} = I_{C2}$), the following equation is obtained.

$$I = 2I_C \left| \cos\frac{\pi\Phi}{\Phi_0} \right| \quad (2.9)$$

Eq. (2.9) means that the current flowing through the SQUID shows an interference pattern such that I is maximized at $\Phi = n\Phi_0$ and becomes zero at $\Phi = n\Phi_0/2$.

On the other hand, in case that the critical currents of the two Josephson junctions are different ($I_{C1} \neq I_{C2}$), the following equation is obtained.

$$I = \left[(I_{C1} - I_{C2})^2 + 4I_{C1}I_{C2}\cos^2\left(\frac{\pi\Phi}{\Phi_0}\right)\right]^{1/2} \quad (2.10)$$

Eq. (2.10) means that the magnetic field response of I shows an interference pattern in which I takes the maximum value $I_{C1} + I_{C2}$ at $\Phi = n\Phi_0$ and the minimum value $|I_{C1} - I_{C2}|$ at $\Phi = n\Phi_0/2$. By measuring such an interference pattern with high accuracy, the

magnetic field can be measured with high resolution. Magnetic moment can be evaluated by measuring the change in magnetic flux when moving the sample.

2.5.2 Data processing of magnetization

Figure 2.11(a) shows a magnetization (*M*) - applied magnetic field (*H*) curve of a typical ferromagnetic thin film. The *M-H* curve shows not only hysteresis originating from ferromagnetic thin film but also linear component derived from the diamagnetism of the substrate. Since the diamagnetism component is proportional to *H*, the *M-H* curve of the ferromagnetic thin film alone (Fig. 2.11(b)) can be obtained by subtracting the linear component (red lines in Fig. 2.11(a)).

M - temperature (*T*) curve also includes a paramagnetic or diamagnetic component from the substrate as the background. I prepared a substrate that experienced the same heat-treatment as the thin film and measured the *M-T* curve of the substrate
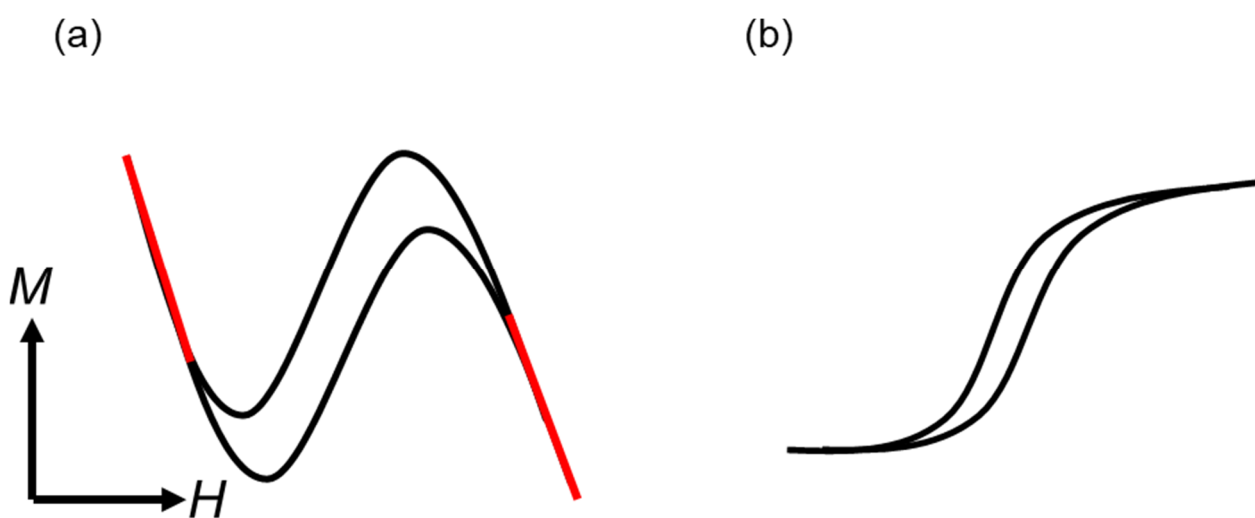

Figure 2.11 Data processing (a)before and (b)after correction.

2.6 Optical measurement

In this study, UV-Vis / NIR Spectrophotometer (UV-vis) manufactured by JASCO Co. Ltd. was used for evaluation of optical properties. The light source can irradiate light with a wavelength of from 200 to 2300 nm

Reflectance R [%] of thin film samples is contributed by the reflection not only at the film surface but also at the back surface, the latter of which can be measured as R_b [%] from back side. On the other hand, when measuring the transmittance, transmittance T [%] was measured by setting the mirror at 180° and evaluating the transmitted light without setting the sample as 100%. In addition to these measurements, the reflectance R_0 [%] of a both-side polished substrate that experienced the same heat-treatment as the thin film was measured.

Each parameter in the optical measurement is calculated as follows [49].

The refractive index of the substrate n_s can be calculated from R_0, using the following equation.

$$n_s = \frac{1 + \sqrt{\dfrac{R_0}{2 - R_0}}}{1 - \sqrt{\dfrac{R_0}{2 - R_0}}} \qquad (2.11)$$

The transmittance T_f [%] and the reflectance R_f [%] of the thin film alone are obtained by the following two formulas

$$T_f = \frac{(1 - R_0)\,T}{1 - 2R_0 + R_0 R_b}, \quad R_f = R - \frac{R_0 T^2}{1 - 2R_0 + R_0 R_b} \qquad (2.12), (2.13)$$

where T is the transmittance measured for the thin film sample.

The refractive index n and the extinction coefficient k of the thin film can be evaluated using the following two formulas.

$$n = \sqrt{\frac{n_s{}^2 T_f + n_s(1+\sqrt{R_f})^2}{T_f + n_s(1-\sqrt{R_f})^2}} \qquad (2.14)$$

$$k = \frac{\lambda}{4\pi t} \ln\left[\frac{(1+n)(n-n_s)+(1-n)(n-n_s)\sqrt{R_f}}{(1-n)(n+n_s)+(1+n)(n+n_s)\sqrt{R_f}}\right] \qquad (2.15)$$

where t is the film thickness and λ is the wavelength of light.

The absorption coefficient α [cm^{-1}] is expressed by the following equation.

$$\alpha = \frac{4\pi k}{\lambda} \qquad (2.16)$$

Based this absorption coefficient, I discuss the electronic structure of solid-state YO.

Chapter 3:
Epitaxial thin film growth of YO, LaO, and GdO*

3.1 Introduction

3.1.1 Why these three *RE*Os?

In this study, to achieve systematic research on solid-state *RE*O, I focused on three *RE*Os, YO, LaO, and GdO. This is because these *RE*Os contain divalent rare-earth ions with one *nd* electron in the outermost, as shown in Table 1.1. Also, considering that these divalent ions have almost equivalent ionic radii, as shown in Fig.1.1, these *RE*Os would take rocksalt structure with close lattice constants. The different point is the electronic structure such as (1) $4d^1$ or $5d^1$ conduction electron in YO and LaO, (2) existence of $4f$ electrons in GdO. Therefore, compared with physical properties of these *RE*Os, effect of the electronic structure can be investigated systematically.

Both YO and LaO are $(d)^1$ systems, but the difference in localization nature between Y $4d$ and La $5d$ possibly affects their electrical transport properties. According to the results of DFT calculation (Fig.1.12), the Y $4d$ or La $5d$ bands should serve as conduction bands. Since La $5d$ electron is more itinerant than Y $4d$ one because of the longer distance from nuclei, LaO epitaxial thin film should have higher carrier density than YO and show metallic behavior like the bulk polycrystal [15]. On the other hand, some of $3d$ transition metal monoxides such as NiO [50] are known as Mott insulators

---

due to the strong localization of $3d$ electron. It is interesting to see whether YO with $4d$ electron is a Mott insulator.

Magnetic properties are also interesting, because Gd^{2+} $((4f)^7(5d)^1)$ has similar electronic configuration to Eu^{2+} $((4f)^7)$. As described in Section 1.2.3, EuO is semiconducting and its Curie temperature (T_c) reaches up to 200 K by carrier doping. On the other hand, GdO is expected to be metallic with higher carrier density than EuO due to the itinerant $5d$ conduction electron like LaO. Therefore, there is a possibility that GdO has much higher T_c than EuO.

In this chapter, I firstly describe epitaxial growth of solid-state REOs. The physical properties of REO (RE = Y, La, Gd) epitaxial thin films are presented in Chapter 4-6. In Chapter 7, I discuss the physical properties of these three REOs in a systematic manner from the view point of the electronic structures.

3.1.2 Synthesis strategy of REO

As described in Section 1.2.1, bulk polycrystals of LaO, CeO, PrO, NdO, and SmO were obtained by high pressure synthesis. However, other REOs could not be synthesized even by high pressure due to the larger formation Gibbs energy. This suggests that it is hard to synthesize them via thermodynamically dominated equilibrium reaction.

Therefore, in this study, I used PLD method for synthesis of REO. PLD method is a kinetically dominated nonequilibrium reaction. As seen from the reaction energy diagram of REO and RE_2O_3 shown in Fig. 3.1, RE_2O_3 is more stable and possesses much smaller Gibbs energy than REO. To avoid the oxidation to highly stable RE_2O_3, ultra-high vacuum condition is needed so that the reaction speed of $RE(g) + O_2(g) \rightarrow RE O(s)$ or $RE O(g) \rightarrow RE O(s)$ should be faster than that of oxidation.
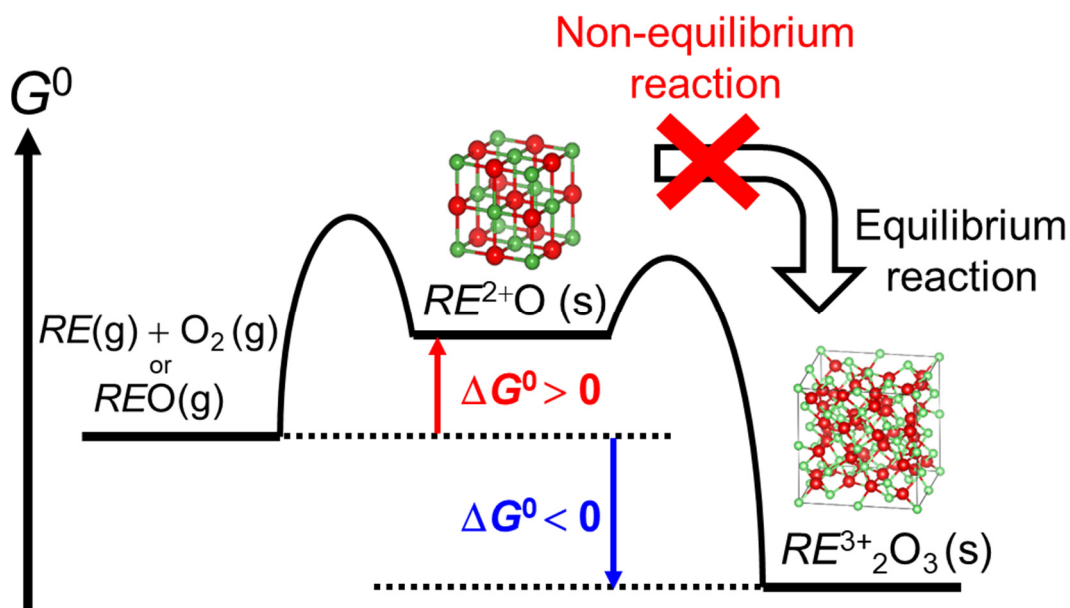
Figure 3.1 Reaction energy diagram of *RE*O and *RE*$_2$O$_3$.

PLD method can meet these conditions; the vacuum level evacuated with a turbo molecular pump is below 10^{-10} Torr, and the reaction speed can be tuned and accelerated by changing pulsed laser frequency. Gaseous *RE*O was observed in the plume generated from solid *RE*$_2$O$_3$ [51]. Thus, *RE*$_2$O$_3$ would be used as a target for synthesizing *RE*O. On the other hand, in the case of EuO, Eu metal has been used as a target [37]. Therefore, selection of target, *RE* metal or *RE*$_2$O$_3$, is an important factor. Selection of substrate is also a key to synthetize *RE*O. When oxide substrate is used, *RE*O may be oxidized due to the oxygen diffusion from substrate.

After examining various combinations of target and substrate, I decided to use *RE*$_2$O$_3$ target and CaF$_2$ substrate for YO and GdO. When oxide substrate was used, only *RE*$_2$O$_3$ thin film was obtained. Use of *RE* metal target produced only *RE* metal thin film. I further optimized various PLD conditions, including optimized laser energy, laser frequency, growth temperature, and oxygen partial pressure. For growth of LaO thin films, I used La metal target and oxide substrate. Growth temperature was found to be a

critical parameter to obtain an epitaxial thin film. Higher substrate temperature tended to cause polycrystalline LaO or La$_2$O$_3$ thin film.

3.2 Experimental

All epitaxial thin films were deposited by pulsed laser deposition method. In the case of YO and GdO, sintered Y$_2$O$_3$ or Gd$_2$O$_3$ pellet was used as a target. As the optimal conditions, YO thin films and GdO thin films were grown at 350 °C on CaF$_2$ (001) ($a =$ 5.4630 Å) substrates using a KrF excimer laser ($\lambda = 248$ nm) and repetition ratio of 15 Hz. The energy density was 1.6 J/cm^2 (YO) or 0.8 J/cm^2 (GdO). Ar 1% O$_2$ mixed gas was introduced during the deposition, in which oxygen partial pressure P_{O2} was controlled from 10^{-11} to 10^{-8} Torr, monitored with quadrupole mass analyzer. A streak pattern of thin films during deposition was observed *in-situ* with RHEED system to confirm the flatness of the film. After deposition, the film surface was capped *in-situ* with an approximately 10 nm thickness AlO$_x$ layer at room temperature to prevent the oxidation. The typical thicknesses of the YO and GdO thin films were 200 nm and 100 nm, respectively.

On the other hand, LaO thin films were deposited on YAlO$_3$ (110) ($a = 5.176$ Å, $b =$ 5.307 Å, $c = 7.355$ Å) substrates and LaAlO$_3$ (001) ($a = 3.79$ Å) substrates. A 99.9% mass La metal pellet was used as a target. All oxide substrates were annealed in air at 1200 °C for 2 h to obtain step-and-terrace structure prior to the film deposition (Fig. 3.2). Pure O$_2$ (5N) gas was introduced during the deposition, in which oxygen partial pressure P_{O2} was controlled from 1×10^{-8} to 4×10^{-8} Torr for varying the amount of oxygen vacancy, monitored with quadrupole mass analyzer. LaO thin films were deposited at 280 °C using a KrF excimer laser with energy density of 1.0 J/cm^2 and repetition ratio of 10 Hz. The streak pattern of LaO thin film during deposition was *in-*

situ observed with RHEED. After deposition, the film surface was capped *in-situ* with about 3 nm AlO$_x$ layer at room temperature to prevent the oxidation. The typical film thickness was approximately 20 nm.
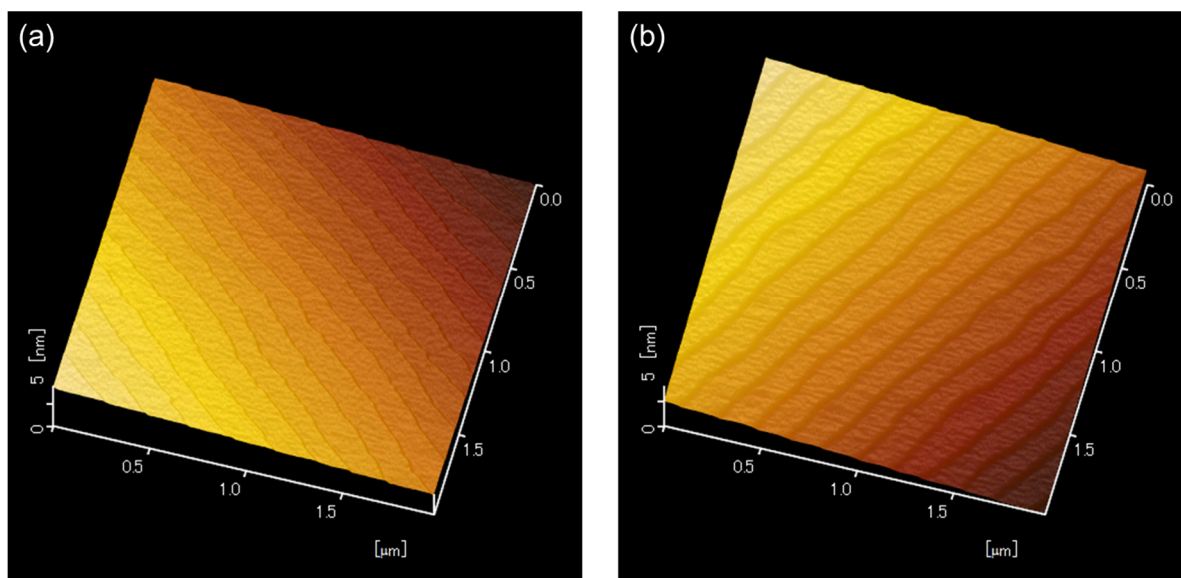

Figure 3.2 Step-and-terrace structure of (a) YAlO$_3$ and (b) LaAlO$_3$ substrates.

RE metal and *RE*$_2$O$_3$ thin films were also deposited as references. Out-of-plane 2θ-ω X-ray diffraction (XRD) measurements and a two-dimensional reciprocal space mapping (RSM) were performed with Cu $K\alpha1$ radiation. In-plane measurements and pole figure measurements were performed with Cu $K\alpha$ radiation. X-ray photoelectron spectroscopy (XPS) with Ar$^+$ sputtering was measured using monochromated Al $K\alpha$ source for depth profile of ionic valence and composition. The XPS peak positions were calibrated by C 1s peak position (284.8 eV).

Y K-edge X-ray absorption near edge structure (XANES) was measured for YO thin films with the bulk-sensitive total fluorescence yield mode at room temperature. The XANES spectra were calibrated by the first peak in the derivative of the Y metal spectrum (17038 eV) [52]. To confirm the crystal structure of YO, transmission electron microscope (TEM) measurement was conducted.

3.3 Results and Discussions

3.3.1 YO

3.3.1.1 Crystal structure analysis of YO

Figure 3.3(a) shows out-of-plane 2θ-ω XRD pattern of the YO film deposited at $P_{O2} =$ 9×10^{-11} Torr. Two peaks at $2\theta = 36.111°$ and $76.574°$ (Fig. 3.3(a)) and a peak at $\chi =$ $35°$ and $2\theta = 31.319°$ were assigned to rocksalt structure YO 002, 004, and 111 diffractions, respectively. α-Y_2O_3 004 and 008 peaks in addition to the forbidden α-Y_2O_3 002 and 006 peaks due to oxygen vacancies [53] were also observed, seemingly indicating surface oxidation of YO film as described below. Fig. 3.3(b) shows a two-dimensional RSM of the same YO film as in Fig. 3.3(a). Both YO and α-Y_2O_3 were fully relaxed but epitaxially grown on CaF_2 substrate with the epitaxial relationships of YO [001] // CaF_2 [001] and YO [100] // CaF_2 [100], respectively (Fig. 3.3(c)). In-plane four-fold symmetry of YO and α-Y_2O_3 was also confirmed by pole figure measurements. Evaluated lattice constants were $a = b = 4.936$ Å and $c = 4.977$ Å with tetragonal distortion $c/a = 1.008$ (inset of Fig. 3.3(a)), showing similar value with those of rocksalt rare earth monoxides LaO (5.144 Å), CeO (5.089 Å), PrO (5.031 Å), NdO (4.994 Å), SmO (4.943 Å), [16] EuO (5.144 Å) [54]. The ionic radius of 6-coordinated Y^{2+} in YO was evaluated to be 1.075 Å from cube root of the cell volume. This value is almost the same as ionic radius of Y^{2+} (1.068 Å) calculated from the Shannon's ionic radius of 6-coordinated Y^{3+} using the empirical formula: Eq.(1.1) [4].
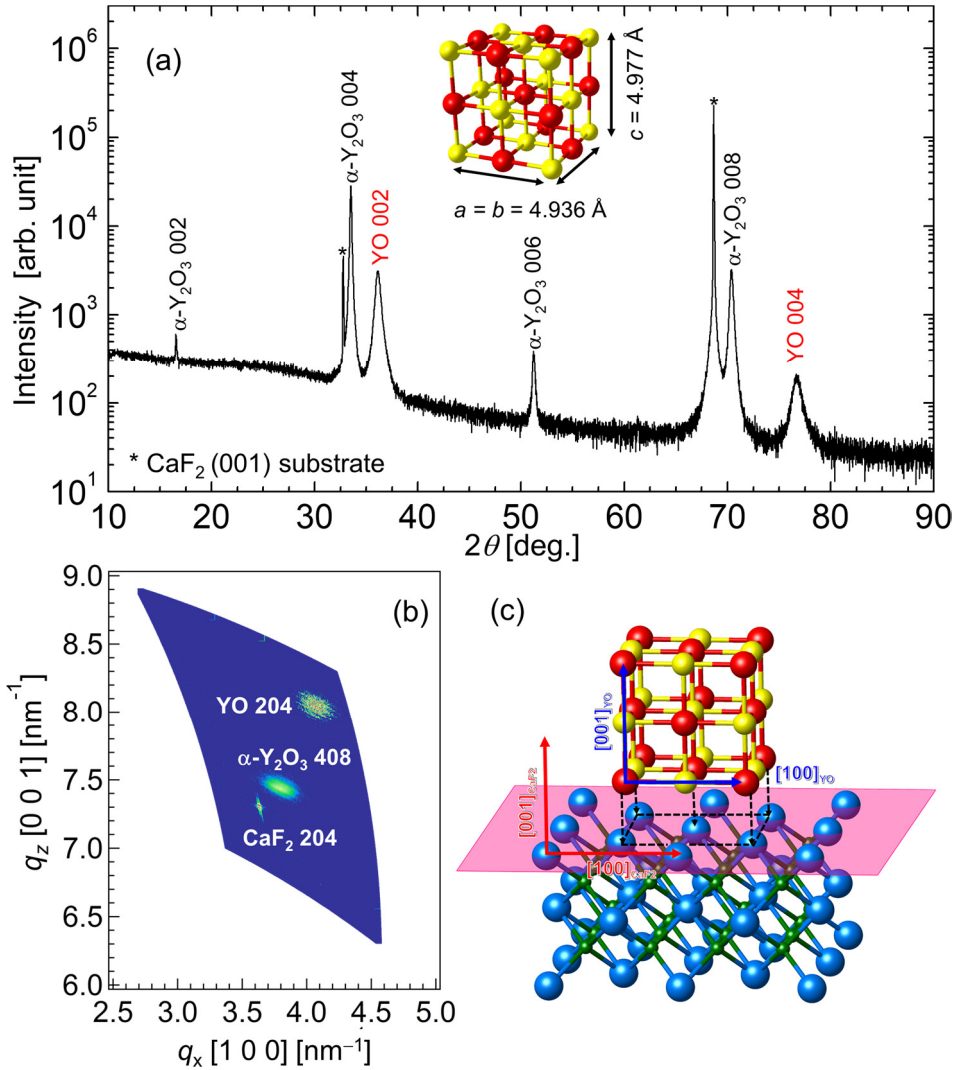
Figure 3.3 (a) out-of-plane $2\theta\text{-}\omega$ XRD pattern of the YO thin film deposited at $P_{O2} = 9 \times 10^{-11}$ Torr. Inset shows crystal structure of YO. (b) a two-dimensional RSM image of YO thin film. (c) Schematic crystal structure of YO thin film on CaF$_2$ substrate.

TEM measurements confirmed epitaxial growth of rocksalt structure YO with a thickness of approximately 180 nm. The surface region with a thickness of ~30 nm was oxidized to Y$_2$O$_3$, even though the sample was capped with a 10 nm AlO$_x$ layer (Fig. 3.4(a)). Figures 3.4 (b) and (c) are magnified images observed in the Y$_2$O$_3$ and YO regions, respectively, clearly resolving the two different structures as highlighted with colored models.
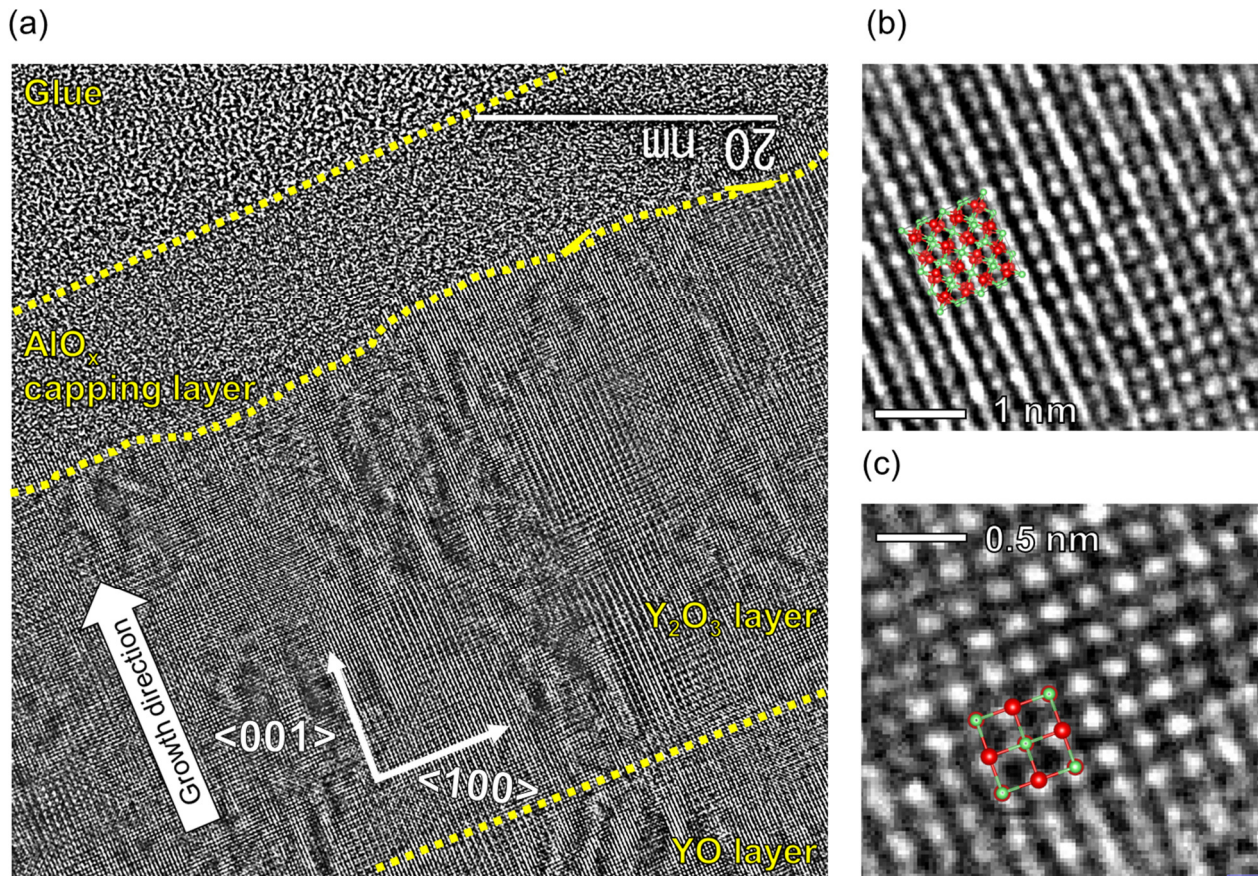
Figure 3.4 (a) A cross sectional TEM image of YO thin film close to the surface (Yellow dot lines indicate boundary of layers). (b),(c) Magnified views of the TEM image with unit cell model of Y_2O_3 and YO.

3.3.1.2 Electronic structure analysis of YO

Figure 3.5(a) shows Y $3d$ XPS spectra for Y metal, YO, and α-Y_2O_3 films. Y metal film showed Y^0 peaks superposed with small Y^{3+} peaks possibly due to oxidation, while α-Y_2O_3 film showed Y^{3+} peaks only. For YO films, Y^{2+} peaks were dominant over Y^0 and Y^{3+} peaks, and the peak position of Y^{2+} at 156.4 eV was almost the same as Y $3d_{5/2}$ peak at 156.5 eV for Y^{2+} in $YH_{2.1}$ [55]. From XPS depth profile, O/Y atomic ratio was approximately 1.0 determined from areal peak intensities of Y $3d$ and O $1s$ inside the

film, while the ratio was almost 1.5 with dominant Y^{3+} ionic state near the film surface (Fig. 3.6), confirming the presence of α-Y_2O_3 layer near the YO film surface.

Figure 3.5(b) shows the Y K-edge XANES spectra for Y metal, YO, and α-Y_2O_3 films. The spectra of YO film showed approximately 1 eV lower absorption edge energy than that of α-Y_2O_3 film, seemingly corresponding to the energy shift from Y^{3+} to Y^{2+}. From these results, solid state YO was proved to possess divalent state.
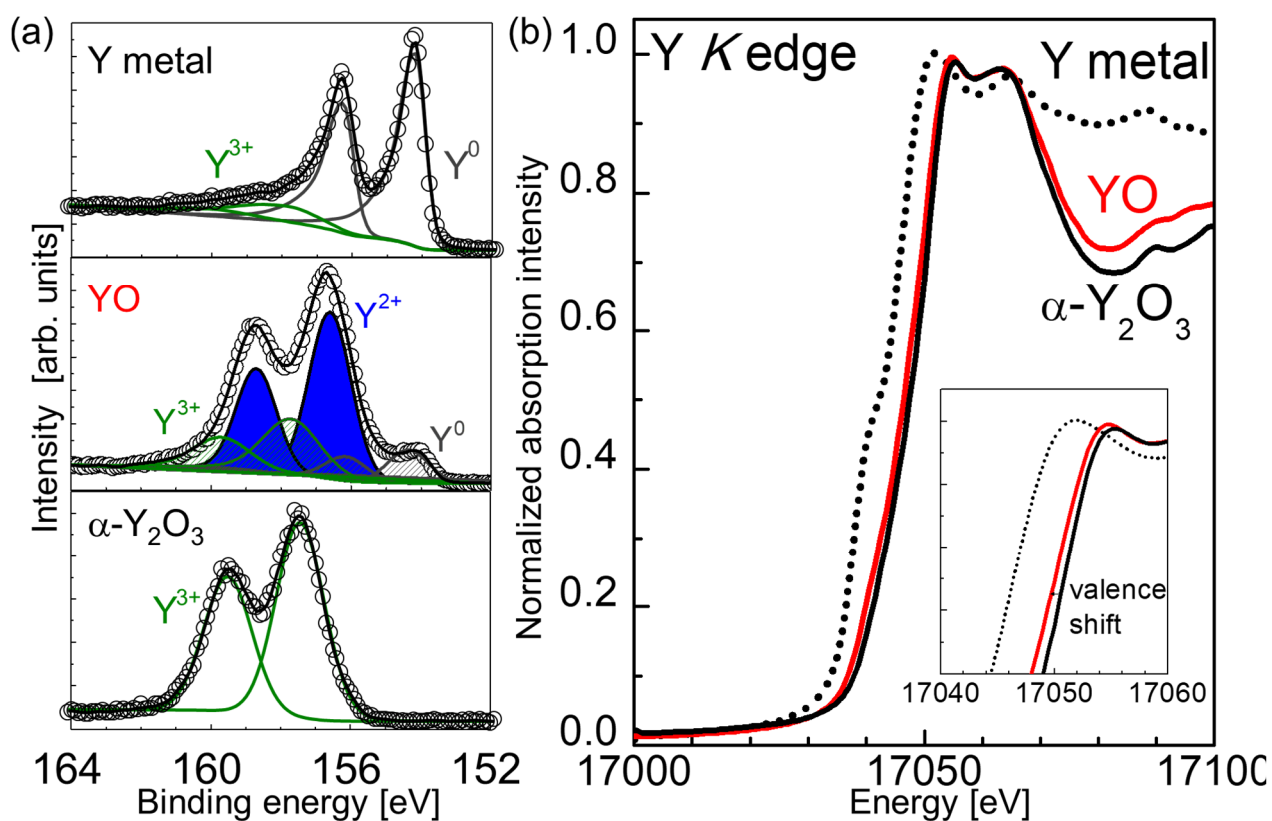
Figure 3.5 (a) Y 3d XPS spectra for Y metal, YO, and α-Y_2O_3 films on CaF$_2$(001) substrates (open symbol). Fitting curves (solid curve) and the deconvoluted Y^0 (gray), Y^{2+} (blue), and Y^{3+} (green) spectra are also shown. (b) XANES spectra at the Y K-edge for Y metal, YO, and α-Y_2O_3 films. Inset shows a magnified view.
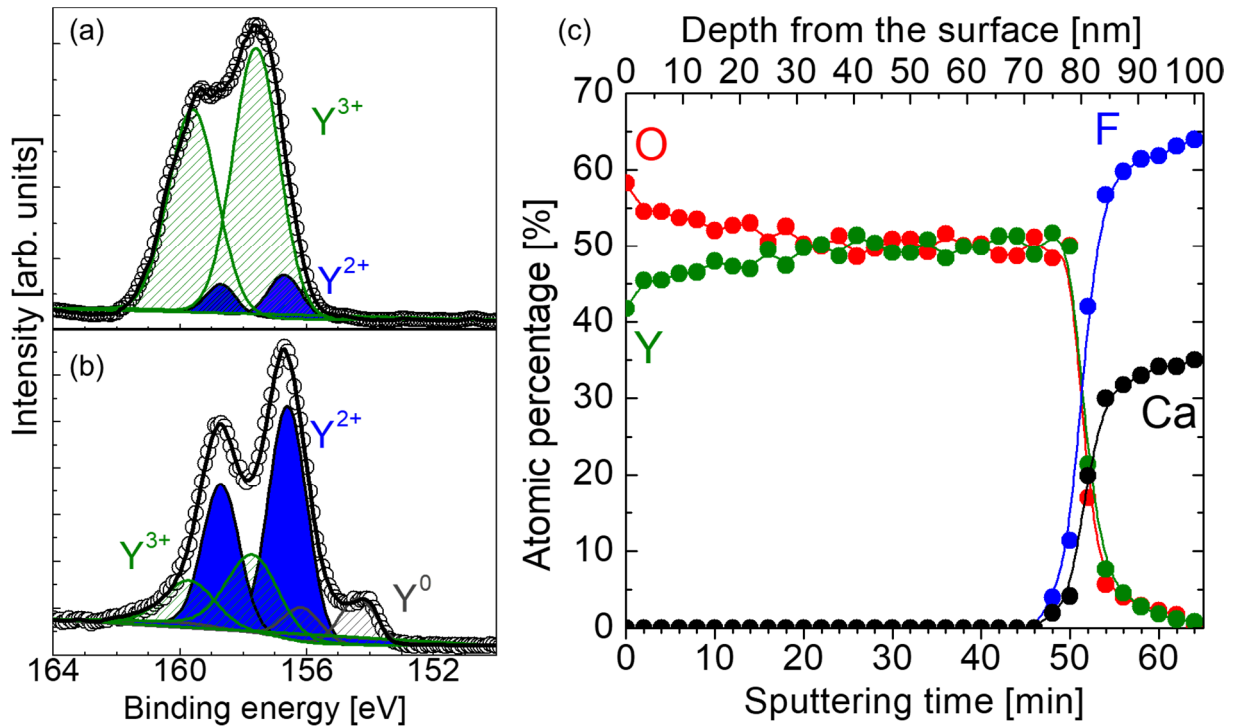
Figure 3.6 (a),(b) Y $3d$ XPS spectra for YO thin film at 10 nm and 40 nm from the surface (open symbol), respectively. Fitting curves (solid curve) and the deconvoluted Y^0 (gray), Y^{2+} (blue), and Y^{3+} (green) spectra are also shown. (b) Depth profile of YO thin film. AlO_x capping layer was removed by Ar^+ sputtering before measurement.

3.3.2 LaO

本節については、５年以内に雑誌等で刊行予定のため、非公開。

3.3.3 GdO

本節については、５年以内に雑誌等で刊行予定のため、非公開。

3.4 Conclusion

I synthesized solid-state YO, LaO, GdO in form of epitaxial thin film via PLD method for the first time, making full use of the characteristics of PLD as a non-equilibrium reaction process.

YO and GdO epitaxial thin films were deposited on CaF_2 substrate by using a RE_2O_3 target. Although these epitaxial thin films were covered with thin RE_2O_3 layers, the surface RE_2O_3 layers were insulating and non-magnetic so their contribution to physical properties was neglected.

LaO epitaxial thin films were grown on oxide substrates by using a La metal target. In contrast to YO and GdO, the LaO films did not contain surface oxidation layer and the crystal quality is comparable to that of well-established EuO epitaxial thin films.

From XRD and XPS measurements, all REO (RE = Y, La, Gd) epitaxial thin films possess rocksalt structure and divalent RE ion. The films are expected to reveal electrical and magnetic properties originating from the divalent states, which will be described in the following chapters.

Chapter 4:
Semiconducting properties of YO*

4.1 Introduction

4.1.1 Previous studies of yttrium oxide

Solid state yttrium oxide has been known as a sesquioxide: Y_2O_3. Y_2O_3 possesses industrially important properties such as high thermodynamic stability (Fig. 1.6), wide band gap (5.5 eV), relatively high dielectric constant ($\varepsilon = 13\text{–}18$), relatively high band offset (2.3 eV) with Si, and good lattice matching with Si (mismatch: −2.4 %) [56,57]. Therefore, Y_2O_3 thin film has been applied for dielectric layers in CMOS devices and high-density dynamic random-access memory (DRAM) [58].

On the other hand, YO has been known as a gaseous phase [59,60], and solid state YO has not been reported so far possibly due to the thermodynamic instability of Y^{2+} (Y^{2+}: $[Kr]4d^1$). In this study, I obtained solid state YO in a form of epitaxial thin film. As a result, its physical properties are obtained for the first time.

4.1.2 Carrier doping with oxygen vacancies

In the case of oxide films, oxygen vacancies (V_O) serve as an electron donor determining the carrier density. One V_O provides two electrons as follows.
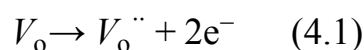
$$V_O \rightarrow V_O^{\cdot\cdot} + 2e^- \quad (4.1)$$

Decrease of oxygen partial pressure during growth (P_{O2}) increases the amount of V_O and then the carrier density. The oxygen vacancy level is formed below the conduction band bottom. Semiconducting conduction turns into degenerate one, i.e. nearly metallic conduction, in case of heavy electron doping as a result of the Fermi level crossing over the conduction band minimum. Thus, tuning P_{O2} by introduction of O_2 or Ar/O_2 mixed gas significantly influences the electrical transport properties of oxide films. Generally, a large amount of V_O expands the lattice volume due to the uncompensated Coulomb repulsion. For example, the lattice constant a_0 of rocksalt titanium monoxide (TiO) was proportional to the amount of V_O ($x < 1$) (Fig. 4.1) [61,62]. In this study, I tuned the carrier density of YO thin films by introducing Ar/O_2 mixed gas, and investigated the effects of P_{O2} on the lattice volume and the physical properties.
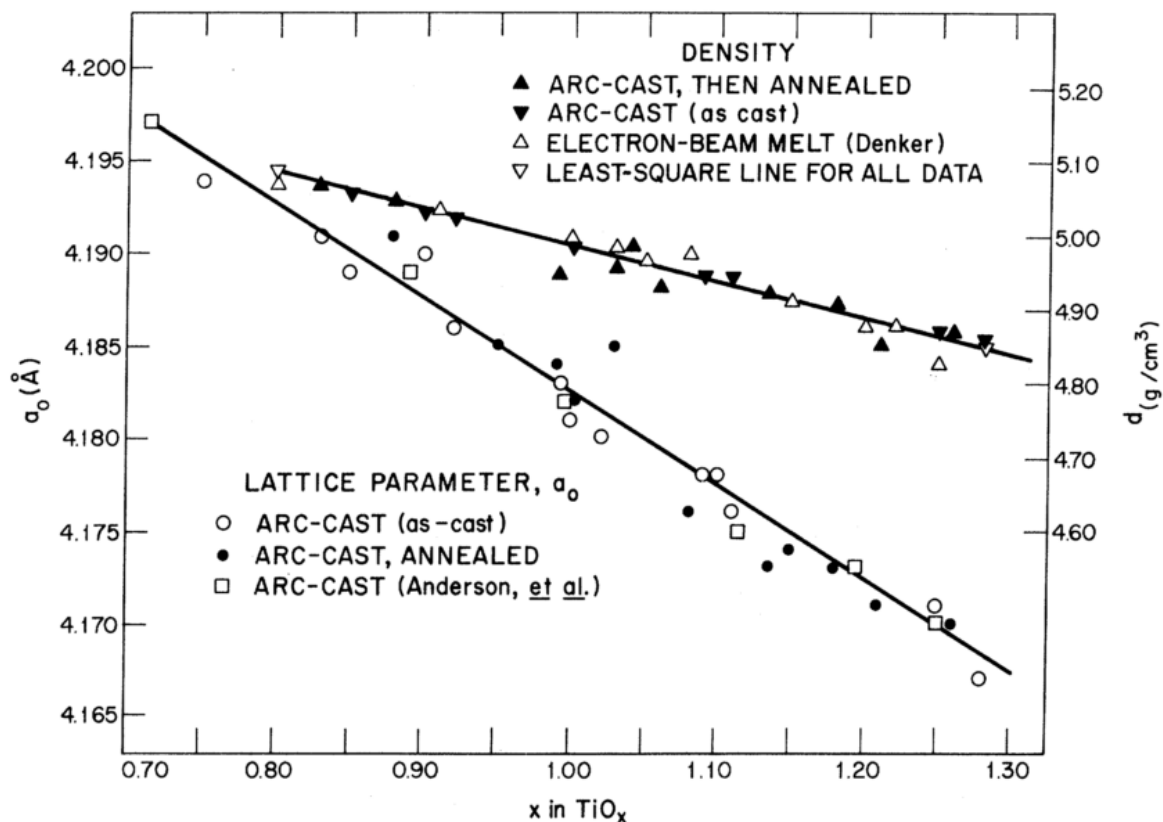
Figure 4.1 Lattice constant a_0 and density d of TiO_x as a function of x. Reprinted with permission from [61]. Copyright 1972 by American Physical Society.

4.2 Methods

As described in section 3.3.1, YO epitaxial thin films were deposited by pulsed laser deposition method. Ar 1% O_2 mixed gas was introduced during the deposition, in which oxygen partial pressure P_{O2} was controlled from 9×10^{-11} to 2×10^{-8} Torr, monitored with quadrupole mass analyzer. Absorption spectra were obtained from transmittance and reflectance. Resistivity and Hall effect were measured using Hall bar-shaped sample with 1 mm width and 3 mm length, where magnetic field was applied perpendicular to the film surface. The carrier density (n) and the mobility (μ) were evaluated at 300 K.

4.3 Results and Discussions

4.3.1 The effects of electron carrier doping on YO

Figure 4.2 shows temperature dependence of resistivity for YO films with different electron carrier density. Similar to TiO [61,62], the carrier density (n) and the lattice constants (a, c) increased monotonically with decreasing P_{O2} (Fig. 4.3(a)). O/Y atomic ratio in YO films decreased monotonically from approximately 1.0 to 0.94 with decreasing P_{O2}, evaluated by XPS depth profile (Fig. 4.3(b)), representing that oxygen vacancies served as electron donor like ordinary oxide semiconductors. The mobility of YO films was about 0.4 cm²/V.s at 300 K. YO film showed higher resistivity than Y
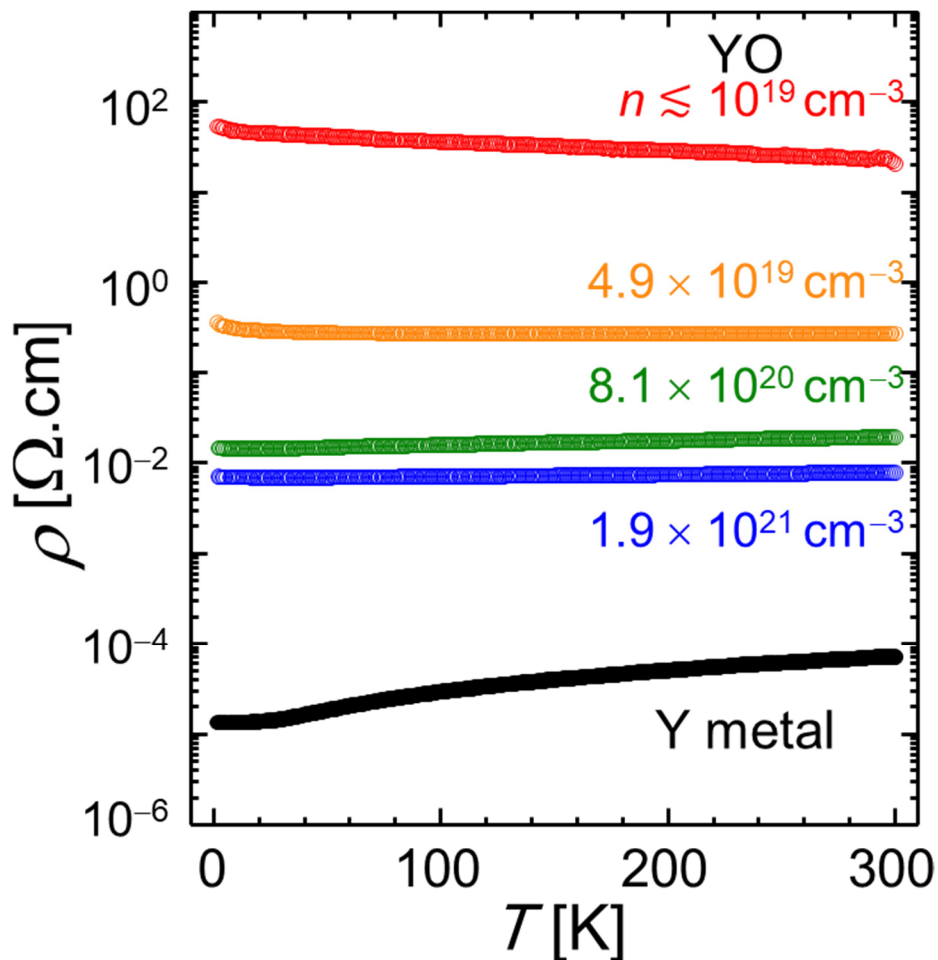
Figure 4.2 Temperature dependence of resistivity for YO films with different electron carrier density. The resistivity of Y metal thin film is also shown as reference.

metal film, showed metallic conduction for $n \geq 10^{20}$ cm^{-3}, and turned to be insulating conduction for $n \leq 10^{20}$ cm^{-3}.
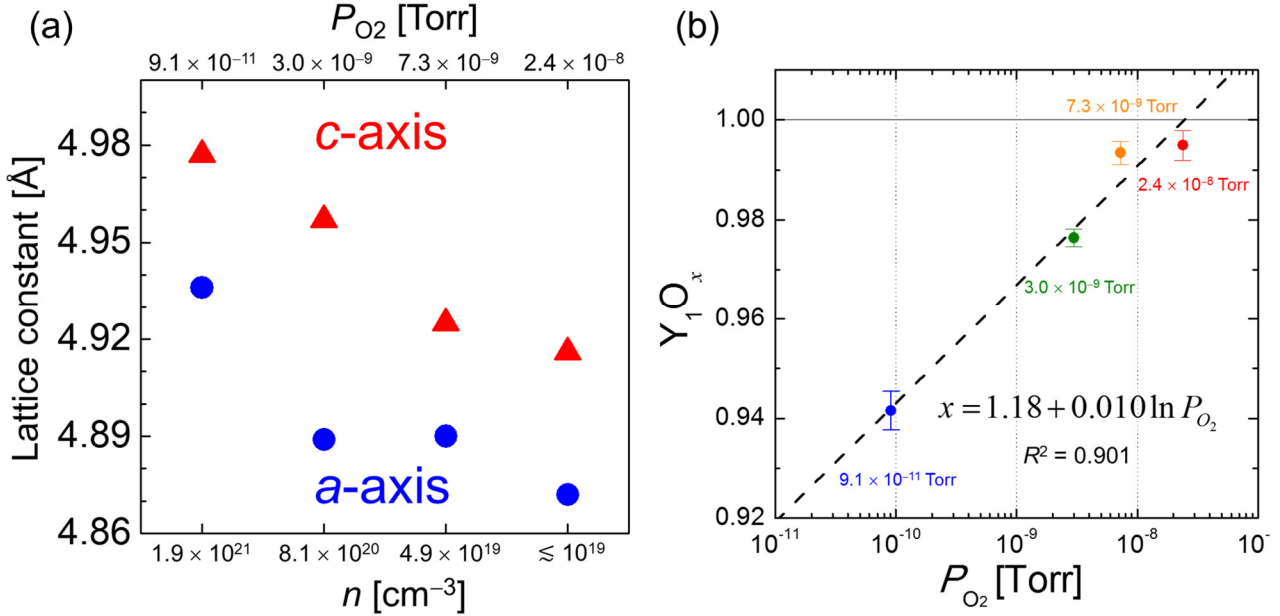
Figure 4.3 (a) Carrier density dependence of lattice constants (*a,c*) and (b) O/Y atomic ratio determined by XPS depth profile for YO films shown in Fig. 4.2.

The resistivity of all the YO films was proportional to $-\log T$ below 20–50 K (Fig. 4.4), suggesting the appearance of the Kondo effect [63]. For example, perovskite SrTiO$_3$ with V_O was reported to show the Kondo resistance minimum [64], and the V_O was plausible cause according to V_O-based Anderson impurity model [63]. Principal carriers in SrTiO$_3$ with V_O are $3d^1$ electron due to Ti^{3+}, while those in YO are $4d^1$ electron, representing the similar electronic configuration. The observed Kondo effect in YO films could be also attributed to the V_O.
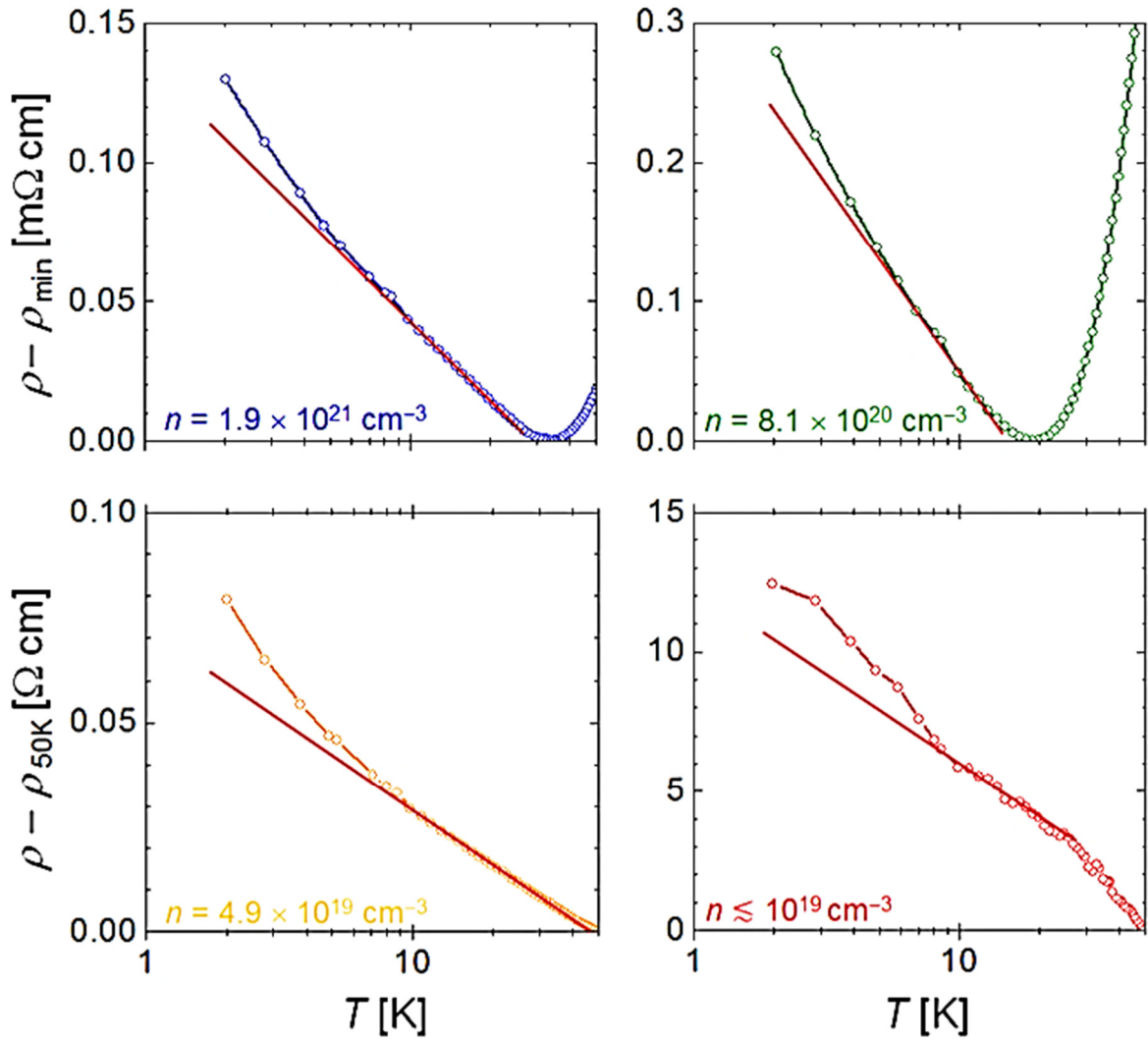
Figure 4.4 Temperature dependence of resistivity below 50 K for the YO films shown in Fig. 4.2.

4.3.2 Strong spin-orbit interaction from Y4d^1 of Y^{2+}

Figure 4.5 shows isothermal magnetoresistance of YO film ($n = 1.9 \times 10^{21}$ cm^{-3}) at different temperature. YO film showed positive magnetoresistance with a sharp dip around 0 T originating from the weak antilocalization effect [65], indicating significant spin-orbit coupling of Y4d orbital. This magnetoresistance was dissimilar to those of Y metal and YH$_2$ films [66], suggesting a different conduction mechanism in YO film.

Similar positive magnetoresistance with a sharp dip was observed in $4d^3$ oxide superconductor: $NbO_{0.98}$ [67] and $5d^4$ Mott insulator: Na_2IrO_3(Fig. 4.6) [68].
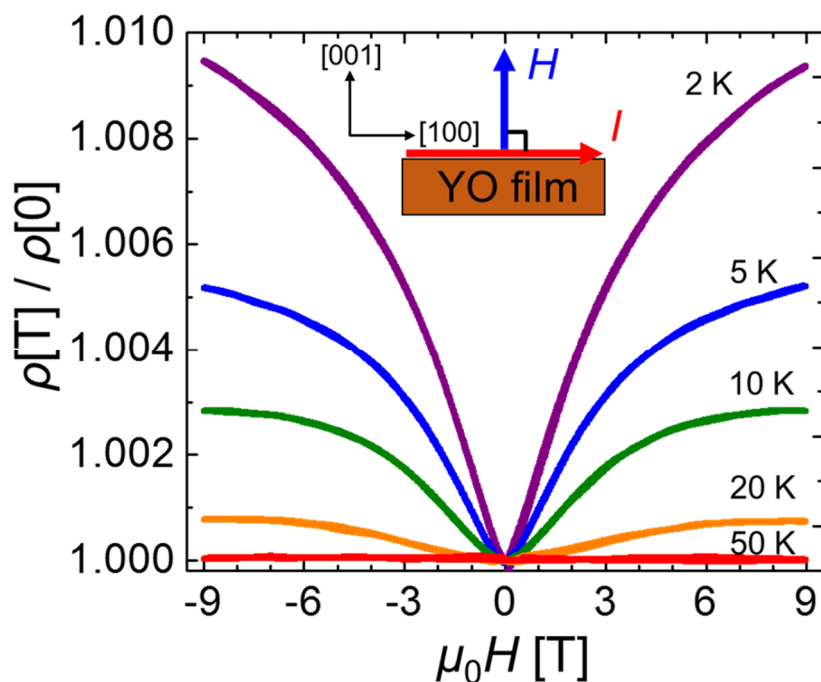
Figure 4.5 Isothermal magnetoresistance of YO film ($n = 1.9 \times 10^{21}$ cm^{-3}) at different temperature. Inset shows the measurement geometry.
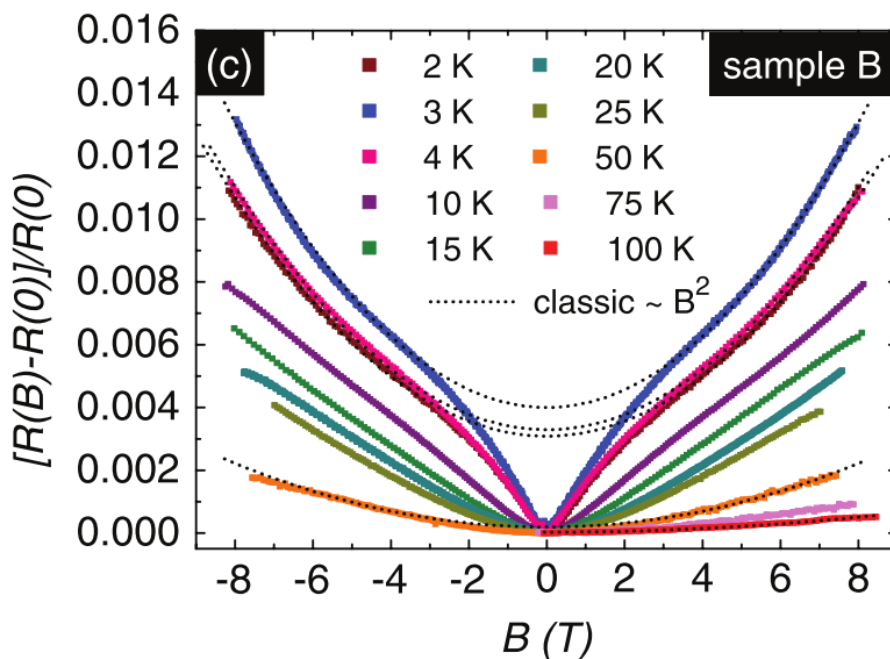

Figure 4.6 Isothermal magnetoresistance of Na_2IrO_3 film at different temperature. Reprinted with permission from [68]. Copyright 2013 by American Physical Society.

4.3.3 Optical properties of YO

Right inset of Fig. 4.7 shows photographs of YO and α-Y_2O_3 thin films. YO was dark brownish in stark contrast with transparent Y_2O_3. Figure 4.7 shows absorption spectra of stoichiometric YO (w/o V_O, $n \leq 10^{19}$ cm^{-3} in Fig.4.2), off-stoichiometric YO (w/ V_O, $n = 1.9 \times 10^{21}$ cm^{-3} in Fig.4.2), and α-Y_2O_3 thin films. α-Y_2O_3 showed sharp absorption edge at 5.6 eV with negligible in-gap absorption. On the other hand, stoichiometric YO showed large and broad absorption at invisible and ultraviolet region with a
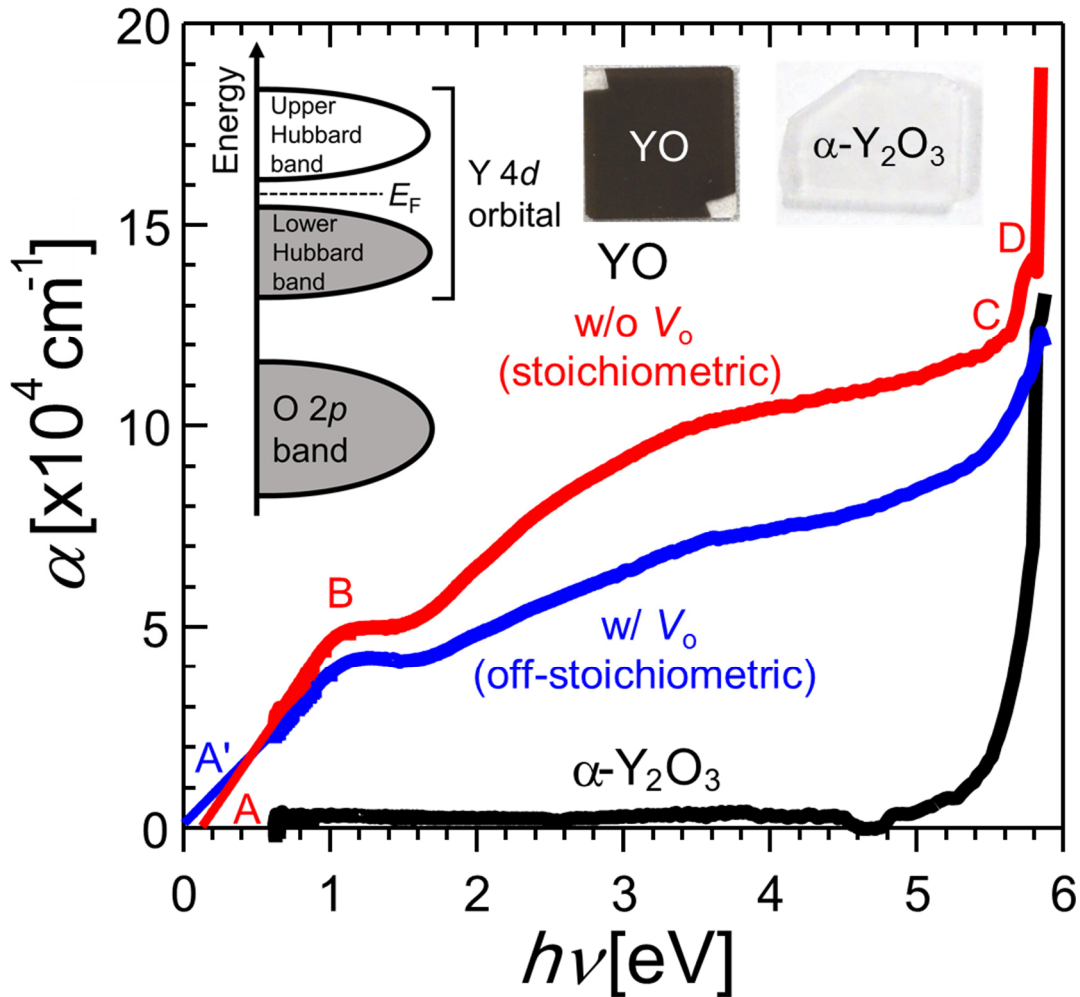
Figure 4.7 The absorption spectra of YO films w/o V_O (stoichiometric, red) and w/ V_O (off-stoichiometric, blue) and α-Y_2O_3 film. Dotted line denotes an extrapolation to estimate band gap. Inset shows schematic energy-band diagram of YO (left) and photographs of YO and α-Y_2O_3 films (right). The indices indicate characteristic energies (see text).

characteristic kink at 1.1 eV (B). Such kink observed in $YH_{1.96}$ was attributed to the presence of octahedral hydrogen site [69], possibly being consistent with the octahedral oxygen site in rocksalt YO structure. Abrupt increase in absorption above 5.8 eV (D) was caused by surface oxidation layer (α-Y_2O_3). A small energy gap around 0.1 eV (A) and an absorption shoulder at 5.6 eV (C) were reminiscent of optical conductivity spectra in Mott insulator $LaTiO_3$ and $YTiO_3$ with $3d^1$ [70], in which the former could be assigned to the Mott gap between lower Hubbard band (LHB) and upper Hubbard band (UHB) and the latter to the charge transfer gap between UHB and $2p$ oxygen band (left inset of Fig. 4.7), possibly caused by $4d^1$ electron correlation in YO.

As shown in Fig. 4.7, the two YO thin films showed similar spectral shape, but the Mott gap was near zero for off-stoichiometric YO thin film (w/ V_O), possibly corresponding to the insulator to metal transition due to electron carrier doping. When the density is nearly one electron per atom, the on-site Coulomb repulsive force between the electrons results in an electron localization in spite of only half-occupied band, corresponding to a strongly correlated electron system. Such localized state is called as Mott insulator. In next section, I discuss the possibility of Mott insulator for YO thin films.

4.3.4 Discussion

When density of electron (hole) carriers is smaller than that of constituent atoms like semiconductors, the carriers can be regarded as spatially extended waves.

Here, let us consider a simple model of only one orbital per atom. In case of band insulator, an up spin and a down spin electrons occupies an atom due to Pauli exclusion principle (Fig. 4.8(a)). In case of Mott insulator, on the other hand, an electron hopping

65

onto neighboring atom is repelled by the on-site Coulomb repulsion (U) (Fig. 4.8(b)). When U is larger than the electron transfer-energy integral (t), electron hopping is prohibited, resulting in an insulating state called as the Mott insulator.
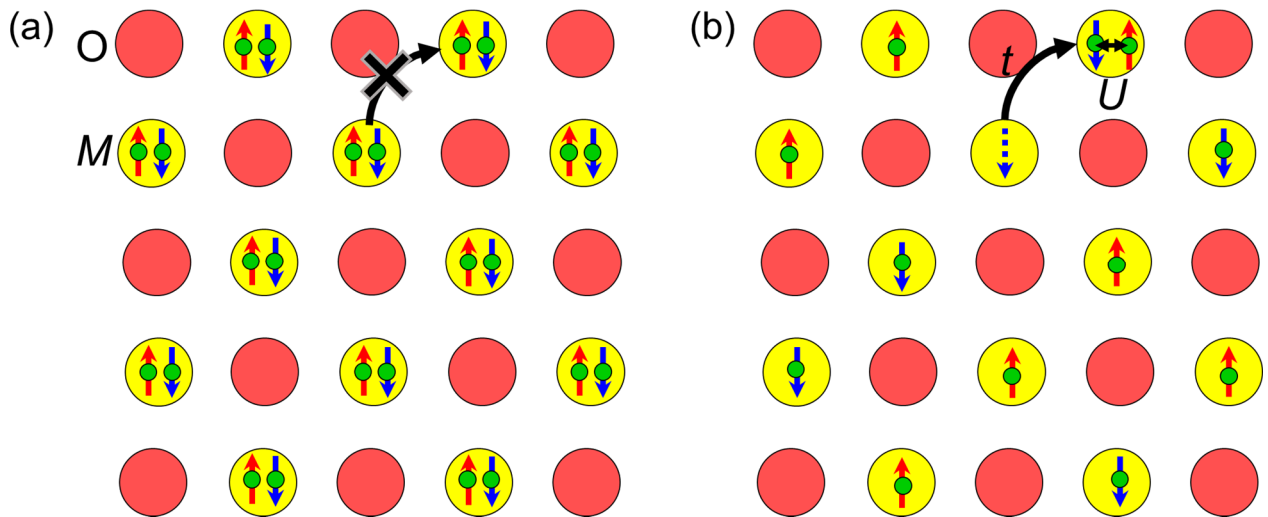

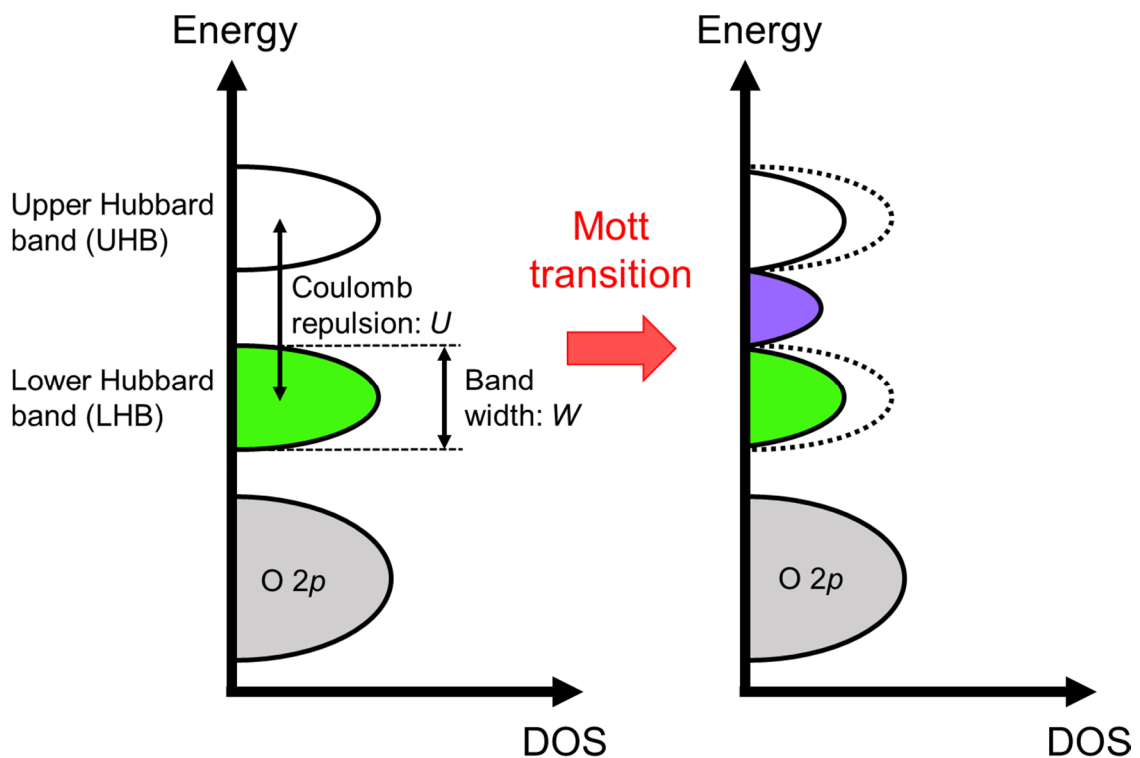Figure 4.8 Schematic images of (a) band insulator and (b) Mott insulator.

Figure 4.9 A schematic image of electronic structure change in Mott transition.

The Mott insulating state is transformed into a metallic state by carrier doping or external stimuli such as magnetic field and light irradiation, corresponding to an insulator to metal transition, which is called as Mott transition. The band (Hubbard) gap between upper Hubbard band (UHB) and lower Hubbard band (LHB) disappears on the insulator to metal transition (Fig. 4.9) [39].

In $3d$ transition metal oxide (TMO), the localized $3d$ state is caused by a large on-site Coulomb repulsion U and a small band width W, resulting in antiferromagnetic Mott insulators seen in stoichiometric $3d$ TMOs (Fig. 4.8(b)) [71]. On the other hand, $4d$ and $5d$ TMOs were considered as weakly correlated wide band systems with largely reduced U due to delocalized $4d$ and $5d$ states [72]. However, anomalously insulating behaviors were recently observed in $4d$ and $5d$ TMOs [73,74,75]. $4d$ TMOs such as $Y_2Ru_2O_7$, $CaRuO_3$, $SrRuO_3$ and $Bi_2Ru_2O_7$ were recognized as Mott insulators residing near the
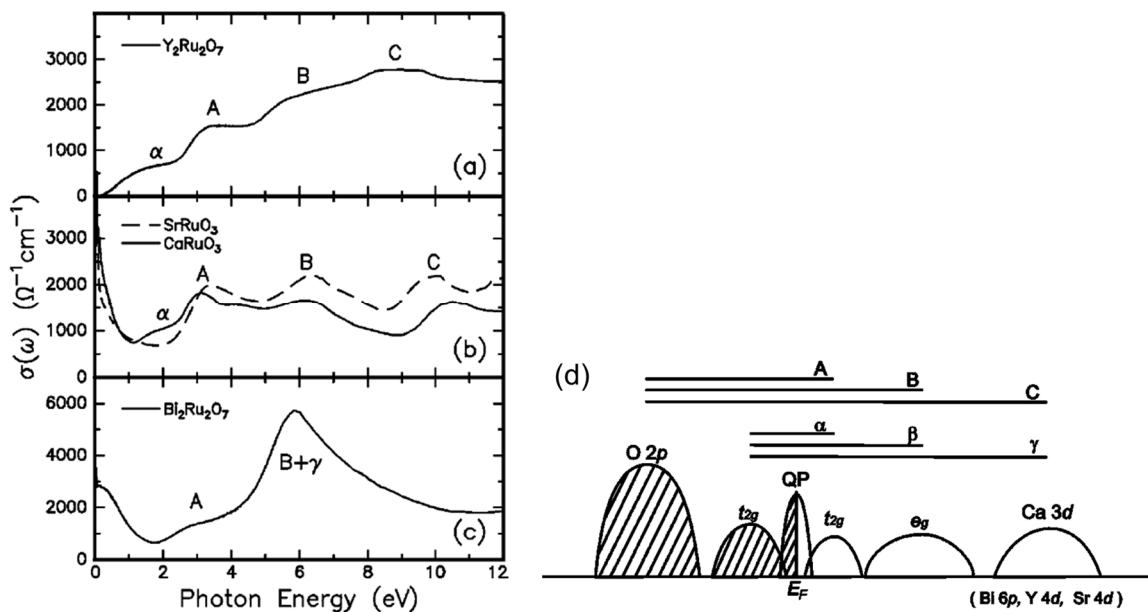

Figure 4.10 Room-temperature optical conductivity spectra $\sigma(\omega)$ of (a) $Y_2Ru_2O_7$, (b) $CaRuO_3$ and $SrRuO_3$, and (c) $Bi_2Ru_2O_7$. The indices correspond to the transitions shown in (d). (d) A schematic diagram of the electronic structures of $CaRuO_3$. Near E_F, the occupied and unoccupied Ru t_{2g} states are located with the QP states at E_F. Reprinted with permission from [76]. Copyright 2001 by American Physical Society.

borderline of the Mott criteria: $U \sim W$ (Fig. 4.10) [72,76]. On the other hand, $5d$ TMOs such as Na_2IrO_3 [64] and Sr_2IrO_4 [77] were considered as Mott insulators due to the strong spin orbit (SO) coupling. Ir $5d$ t_{2g} band split into effective total angular momentum $J_{eff} = 1/2$ doublet and $J_{eff} = 3/2$ quartet bands due to the SO coupling (Fig. 4.11). Sr_2IrO_4 showed the insulator-metal transition triggered by doping electron carriers [78].

Taking into account the optical absorption and electrical transport properties, YO could be regarded as a Mott insulator because of the d^1 electron configuration and/or the strong spin orbit (SO) coupling similar to $4d$ and $5d$ TMOs. Several $3d$ transition-metal monoxides such as MnO [79] and NiO [80] are Mott insulators, but $4d$ metal monoxides have been scarcely identified as the Mott insulator. In order to confirm this scenario, more evidences would be required in future studies.
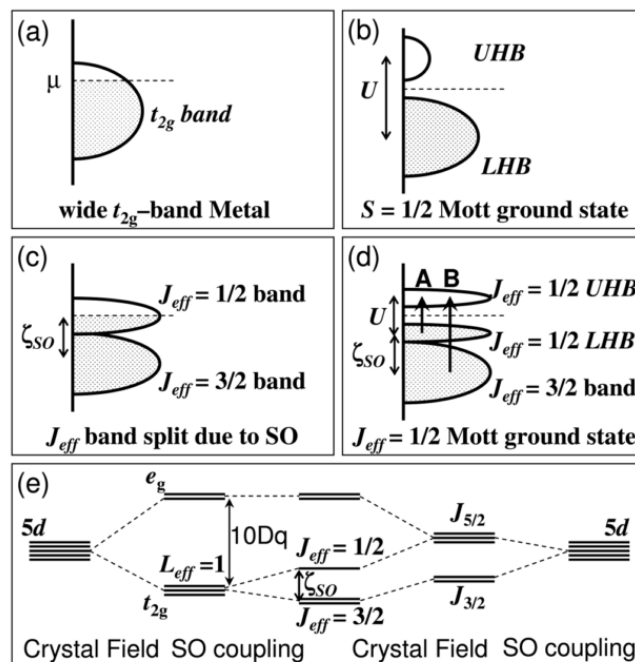

Figure 4.11 Schematic energy diagrams for the $5d^5$ (t_{2g}^5) configuration (a) without SO and U, (b) with an unrealistically large U but no SO, (c)with SO but no U, (d) with SO and U. (e) $5d$ level splitting by the crystal field and SO coupling. Reprinted with permission from [77]. Copyright 2008 by American Physical Society.

4.4 Conclusion

In summary, I synthesized solid state rocksalt YO with unusual valence Y^{2+} in the form of epitaxial film. Solid state divalent rare earth monoxides have been scarcely synthesized in contrast with various divalent rare earth complexes recently synthesized [2,81].

YO film was a narrow gap semiconductor with dark brown color, and the electrical conductivity was widely tuned like ordinary oxide semiconductors. In addition, the absorption spectrum implies the characteristic of Mott insulator, possibly reflecting $4d^1$ electron correlation in YO. So far, few $4d$ metal monoxides have been synthesized and the Mott insulating state has never been reported. Even delocalized $4d$ metal monoxides could become Mott insulators due to the strong spin orbit coupling and/or the electron configuration.

Chapter 5:
Superconductivity of LaO

本章については、５年以内に雑誌等で刊行予定のため、非公開。

Chapter 6:
Room temperature ferromagnetism of GdO

本章については、５年以内に雑誌等で刊行予定のため、非公開。

Chapter 7:
General conclusion

In this thesis, I synthesized solid state *RE*O in a form of epitaxial thin film using PLD method to unveil its physical properties, because solid state *RE*O has been scarcely investigated mainly because of the thermodynamic instability of divalent *RE* ion. Thanks to kinetic growth nature of PLD method, I discovered various fascinating phenomena in divalent *RE*O epitaxial thin films.

To achieve systematic research on solid-state *RE*O, I focused on three compounds, YO, LaO, and GdO. This is because these *RE*Os possess divalent rare-earth ions with one *nd* electron in the outermost shell and would take rocksalt structure with close lattice constants. Meanwhile, there is a remarkable different point in the electronic structure, such as (1) $4d^1$ and $5d^1$ conduction electron in YO and LaO, respectively, (2) existence of $4f$ electrons in GdO. The influence of electronic structure on physical properties of these *RE*Os, was systematically investigated.

Firstly, YO epitaxial thin film was found to be a narrow gap semiconductor with dark-brown color, and the electrical conduction could be widely tuned by the oxygen content, similar to conventional oxide semiconductors. In addition, characteristic Mott insulator-like behavior was observed from optical measurements. There is a possibility that strong spin orbit coupling play a role in the behavior.

Secondly, LaO epitaxial thin film was found to be a new superconductor with onset superconducting T_c around 5 K, which is the highest among lanthanum monochalcogenides against the chemical trend of T_c: 0.84 K, 1.02 K, and 1.48 K for La*X* (*X* = S, Se, Te), respectively. The carrier control resulted in a dome-shaped T_c as a

function of electron carrier density, where the carriers originated from the $5d^1$ electron of La^{2+} and oxygen vacancies. Surprisingly, T_c was very sensitive to epitaxial strain: 4.56 K for compressive-strained film on $YAlO_3$ substrate and 5.24 K for tensile-strained film on $LaAlO_3$ substrate.

Thirdly, GdO was found to be a new room temperature ferromagnetic semiconductor with $T_C \approx 320$ K, which is the highest value among Gd-based binary compounds. The electrical conduction was tunable with the amount of oxygen vacancies. The $4f^7 5d^1$ electron configuration of divalent Gd ion possibly enhances the Curie temperature through RKKY interaction.

In this way, solid state REO with simple rocksalt structure shows various fascinating electrical and magnetic properties such as superconductivity and room temperature ferromagnetism, demonstrating rich electronic features of divalent RE ion hybridized with O ion.

The main achievements in this study were establishment of epitaxial thin film growth technology for rocksalt rare earth monoxides and discovery of novel functionalities. The former would be readily applicable to other rare earth monoxides, suggesting discovery of other functionalities. Simple rocksalt structure is also useful as a building block in layered oxides heterostructures. Thus the present achievements could not only expand the range of functional transition metal oxides but also contribute to the design of novel oxide materials that usie a wide variety of building components.

Acknowledgements

This study has been supported by a lot of persons involved in my research. After graduating from Tokyo Institute of Technology (Titech) in 2013, my five years' research life as a student in University of Tokyo consisted of various priceless experiences (and tremendous hardships) thanks to their helps. Especially, through the fascinating research on superconductivity of LaO, my perspective has largely changed, and I determined to be a scientist as lifework.

First, I would like to appreciate to my supervisor Prof. Tetsuya Hasegawa for providing me an opportunity of the wonderful research life. If I had not chosen Univ. Tokyo at that time in 2013, perhaps REO would have been veiled and I would not have made up my mind to live as a scientist from now on. Surely, my successfully performed study in Ph.D course was grateful to his great supports thorough exciting discussion and precise comments.

Also, I would like to show greatest appreciation to Prof. Tomoteru Fukumura for his insightful advises and constructive suggestions. Without him, my research on REO would have not been fruited. He taught me the basics of scientific research. In addition, in the first two years of Ph.D course, I got nice experience involved in the start-up of his laboratory in Tohoku University to the best of my poor abilities.

I would like to express special thanks to Dr. Daichi Oka, Dr. Taniyuki Furuyama, Dr. Hideyuki Kawasoko, Dr. Hirofumi Oka, and Ms. Madoka Suzuki, who are/were the staffs in Fukumura laboratory. Thanks to them, I had a fruitful research life in Sendai. Especially, Dr. D. Oka supported me on conducting various experiments with his deep knowledge and skill.

I would like to deeply apologize to Prof. Akira Ohtomo for not having chosen your laboratory. I really respect you for your accomplishments, especially as a pioneer of 2D interface in heterostructure. In some days, I am looking forward to working together again.

Finally, I am grateful to my family and friends for their warm understandings for my research work. As my gratitude, someday I hope that my accomplishments will surely lead to improvement of their daily lives.

December 18th, 2017

<div align="right">Kenichi KAMINAGA</div>

References

[1]足立吟也, 入門 レアアースの化学 (化学同人, 2015).

[2] G. Meyer, *Angew. Chem. Int. Ed.,* **53**, 3550-3551 (2014).

[3] R.D. Shannon, *Acta Cryst*., **A32**, 751-767 (1976).

[4] Y.Q. Jia, *J. Solid State Chem.*, **95**, 184-187 (1991).

[5] G.R. Giesbrecht *et al., Dalton Trans*., **16**, 2387-2393 (2004).

[6] S. Cotton, 希土類とアクチノイドの化学 (丸善, 2008).

[7] G. Adachi *et al., Chem. Rev.,* **98**, 1479-1514 (1998).

[8] M. Zinkevich, *Prog. Mater. Sci.,* **52**, 597-647 (2007).

[9] M. W. Shafer *et al., J. Phys. Chem. Solids* **33**, 2251 (1972).

[10] I. Katayama *et al., Kidorui* **25**, 19 (1994).

[11] A.V. Prokofiev *et al., J. Alloys Compd.*, **242**, 41-44 (1996).

[12] R. Ivanic *et al., J. Electr. Eng.* **54**, 83 (2003).

[13] A.E. Miller *et al., J. Chem. Phys.,* 55, 2647 (1971).

[14] G. Krill *et al., Solid State Commun.,* **33**, 351-353 (1980).

[15] J.M. Leger *et al., Phys. Lett.,* **80A**, 325 (1980).

[16] J.M. Leger *et al., J. Solid State Chem.,* **36**, 261-270 (1980).

[17] T.L. Felmlee *et al., Inorg. Chem.*, **7**, 660 (1968).

[18] G.J. Mccarthy *et al., J. Less Common Metals*, **22**, 409 (1970).

[19] G. Brauer *et al., Z. Anorg. Allg. Chem.*, **356**, 46 (1967).

[20] M. Shafiq *et al., J. Alloys Compd.*, **618**, 292-298 (2015).

[21] J.O. Dimmock *IBM J. Res. Dev*. **14**, 301-308 (1970).

[22] V. Eyert *et al., Solid State Commun*., **60**, 905-911 (1986).

[23] A. Mauger *et al., Phys. Rep.* **141**, 51-176 (1986).

[24] P.G. Sterrneken *et al., Phys. Rev. Lett*. **88**, 047201 (2002).

[25] A. Schemehl *et al., Nat. Mater*. **6**, 882 (2007).

[26] G. Petrich *et al., Phys. Rev. Lett.* **26**, 885 (1971).

[27] M. W. Shafer *et al., J. Phys. Chem. Solids* **33**, 2251 (1972).

[28] N.J.C. Ingle *et al., Phys. Rev. B* **77**, 121202(R) (2008)

[29] X. Wan *et al., Phys. Rev. B* **83**, 205201 (2011).

[30] H. Miyazaki *et al., Appl. Phys. Lett*. **96** 232503 (2010).

[31] R. Sutarto *et al. Phys. Rev. B* **80**, 085308 (2009).

[32] A. Melville *et al. Appl. Phys. Lett.* **100**, 222101 (2012).

[33] J.M. An *et al., Phys. Rev. B* **88**, 054421 (2013).

[34] X. Wang *et al. IEEE Trans. Magn.* **46**, 1879–1882 (2010).

[35] A. Melville *et al. Appl. Phys. Lett.* **102**, 062404 (2013).

[36] S. B. Ogale, T. V. Venkatesan, and M. Blamire, Functional Metal Oxides: New Science and Novel Applications (John Wiley & Sons, 2013).

[37] T. Yamasaki *et al., Appl. Phys. Lett.* **98**, 082116 (2011).

[38] Y. Ohuchi *et al., Phys. Rev. Lett.* **91**, 245115 (2015).

[39] 澤彰仁, 酸化物薄膜・接合・超格子　界面物性と電子デバイス応用 (内田老鶴圃, 2017).

[40] 吉田貞史・近藤高志, 薄膜工学 [第 2 版] (丸善出版, 2011)

[41] J. Wei *et al., Cryst. Growth Des.* **15**, 2187-2191 (2015).

[42] 日本表面科学会, ed., 透過型電子顕微鏡 (丸善出版, 2009).

[43] 日本表面科学会, ed., ナノテクノロジーのための走査プローブ顕微鏡 (丸善出版, 2002).

[44] 日本表面科学会, ed., X 線光電子分光法 (丸善出版, 1998).

[45] A. Cros, *J. Electron Spectrosc. Relat. Phenom.* **59**, 1 (1992).

[46] 高橋 隆, 光電子固体物性 (朝倉書店, 2011).

[47] 大塚洋一, 小林俊一, eds, 丸善実験物理学講座(11) 輸送現象測定 (丸善出版, 1999).

[48] 日本化学会, ed., 第 5 版実験化学講座 7 電気物性,磁気物性(丸善出版, 2004).

[49] 小檜山光信, 光学薄膜の基礎理論 増補改訂版 (オプトロニクス社, 2011).

[50] V.I. Anisimov *et al., Phys. Rev. B* **44**, 943 (1991).

[51] J.M. Badie *et al., Chem. Phys. Lett.* **364**, 550-555 (2002).

[52] J. A. Bearden *et al., Rev. Mod. Phys*. **39**, 125 (1967).

[53] M. G. Paton *et al., Acta Cryst.* **19**, 307 (1965).

[54] H. A. Eick *et al., J. Am. Chem. Soc.* **78**, 5147 (1956).

[55] A. Fujimori *et al., J. Phys. C: Solid State Phys.* **17**, 341 (1984).

[56] J.J. Chambers *et al., J. Appl. Phys.* **90**, 918 (2001).

[57] J. Roberston, *Vac. Sci. Technol. B* **18**, 1785 (2000).

[58] K. Nomura *et al, Jpn. J. Appl. Phys.* **45**, 4303 (2006).

[59] R.J. Ackermann *et al., J. Chem. Phys*. **40**, 883-889 (1964).

[60] W.J. Childs *et al., J. Chem. Phys*. **88**, 598-606 (1988).

[61] M.D. Banus *et al., Phys. Rev. B* **5**, 2775 (1972).

[62] J. Hulm *et al., J. Low Temp. Phys*. **7**, 291 (1972).

[63] C. Lin *et al., Phys. Rev. Lett.* **111**, 217601 (2013).

[64] M. Lee *et al., Phys. Rev. Lett.* **107**, 256601 (2011).

[65] P.A. Lee *et al., Rev. Mod. Phys.* **57**, 287 (1985).

[66] M. Sakai *et al., J. Appl. Phys.* **101**, 103713 (2007).

[67] J. Honig *et al., J. Solid State Chem.*, **6**, 203 (1973).

[68] M. Jenderka *et al., Phys. Rev. B* **88**, 045111 (2013).

[69] J.H. Weaver *et al., Phys. Rev. B* **19**, 4855 (1979).

[70] T. Arima *et al., J. Phys. Soc. Jpn.* **64**, 2488 (1995).

[71] M. Imada *et al., Rev. Mod. Phys.* **70**, 1039 (1998).

[72] W.D. Ryden *et al., Phys. Rev. B* **1**, 1494 (1970).

[73] S. Nakatsuji *et al., Phys. Rev. Lett.* **84**, 2666 (2000).

[74] M.K. Crawford *et al., Phys. Rev. B* **49**, 9198 (1994).

[75] D. Mandrus *et al., Phys. Rev. B* **63**, 195104 (2001).

[76] J.S. Lee *et al., Phys. Rev. B* **64**, 245107 (2001).

[77] B.J. Kim *et al., Phys. Rev. Lett.* **101**, 076402 (2008).

[78] O.B. Corneta *et al., Phys. Rev. B* **82**, 115117 (2010).

[79] J. Kuneš, *et al. Nat. Mater.* **7**, 198-202 (2008).

[80] V.I. Anisimov *et al., Phys. Rev. B* **44**, 943 (1991).

[81] M.R. MacDonald *et al., J. Am. Chem. Soc.* **133**, 15914 (2011).